FINAL TECHNICAL REPORT

ONR Grant N00014-89-J-1483

SEISMIC ANISOTROPY AND LARGE-SCALE POROSITY IN THE OCEAN FLOOR

Institution: Hawaii Institute of Geophysics
                        University of Hawaii at Manoa
                        2525 Correa Road
                        Honolulu, HI 96822

DTIC
ELECTE
APR 13 1990
S D
D

90 04 11 132

FINAL TECHNICAL REPORT

Seismic Anisotropy and Large-Scale Porosity in the Ocean Floor
N00014-89-J-1483
1 January 1989 – 31 December 1989

Gerard J. Fryer, P.I.
Hawaii Institute of Geophysics
University of Hawaii at Manoa
2525 Correa Road
Honolulu, HI 96822

Rationale for the Study

Fracturing, flow layering, brecciation, and vesiculation in the lavas forming the uppermost igneous crust result in high porosity and induce an elastic anisotropy. Anisotropy resulting from horizontal fracturing or interbedded horizontal lava flows displays no azimuthal dependence, making it hidden to traditional seismology and inviting misinterpretation of seismic data. Porosity too seems poorly constrained by seismic data, largely because of inadequacies in existing theoretical velocity-porosity relationships. Fracture-induced anisotropy and large-scale porosity, however, must be strongly affected by ocean-floor processes such as hydrothermal deposition and crustal ageing. This project was one in a continuing series of ONR-funded projects to assess the seismic effects of this anisotropy and porosity, to see if these properties can be deduced from field seismic measurements, and to explore how they might be used to investigate bottom processes.

Project Objectives

This project had two specific goals. Under previous ONR support (Contract N00014-87-K-0181) we had claimed that measurement of anisotropy can be accomplished seismically if both source and receiver are on the bottom, provided that both *SH* and *SV* information is obtained. We wished to verify this claim using data from a high-resolution shallow water experiment run by Rondout Associates and Woods Hole Oceanographic Institute using on-bottom sources and three-component receivers (only if we could demonstrate our abilities on shallow-water sediments could measurement on deep-water crust be contemplated). During 1988 we had managed to model the horizontal geophone data from one line by invoking transverse isotropy in the bottom, but without also explaining the vertical data our claim for anisotropy was unconvincing. We wished to refine our models so that all seismic energy was adequately explained.

The second objective was to refine our understanding of velocity-porosity relationships in volcanic ocean floor. In 1988 we presented an explanation of how hydrothermal sealing of cracks and fractures can explain the rapid increase in seismic velocities with age in young igneous crust by modifying the mean void aspect ratio, but that explanation was purely qualitative. We wished to tighten the theory, predict some hard numbers from it, and see if our explanation could withstand comparison with ocean drilling results.

EFFECT OF ASPECT RATIO ON BASALT VELOCITY

Figure 1: *P*-velocity versus porosity for different aspect ratios alpha.

Accomplishments

Our analysis of the Rondout/WHOI shallow water data is now complete. Through iterative match of synthetic seismograms to data we have been able to match all three components on two crossing lines using the same transversely isotropic structure, demonstrating that ocean bottom anisotropy *can* be measured without resorting to downhole seismometers. The anisotropy demanded by the data is large (*P*-wave speed variation of 12%), but is entirely consistent with the bottom being made up of interbedded sand and silty clays. A paper describing this work has been submitted to *Geophysical Journal International,* where it is currently in review. A preprint of this paper is included as the Appendix to this report.

Our theory of crustal ageing is advancing and is necessarily expanding into an assessment of depth-dependent variation as well. Our basic idea is this: in volcanic crust, which has void space varying from thin fractures to the much more equidimensional interstices between pillows, hydrothermal mineralization seals the thin voids first so that the mean aspect ratio increases with time (i.e., void space becomes more circular). Porosity resulting from narrow voids has a very strong effect on velocity (Figure 1). When there is a distribution of aspect ratios, sealing the narrowest voids will reduce porosity only slightly but will dramatically increase the velocity. Such change of mean aspect ratio, both with depth and with age, is strongly supported by sonic and neutron porosity logs from the drilling program. At site 504B (6 Ma), we find that the velocity varies less and less rapidly with porosity as depth increases (Figure 2), suggesting a downhole increase in the mean aspect ratio. At the much older Site 418A (110 Ma), within the 400 m of basement logged, all depths display the same velocity-porosity relationship as is found at about 400 m into basement at 504B (although porosities themselves still systematically decrease downhole). If the crust at 418A ever evolved through a 504B-like stage, then there

2
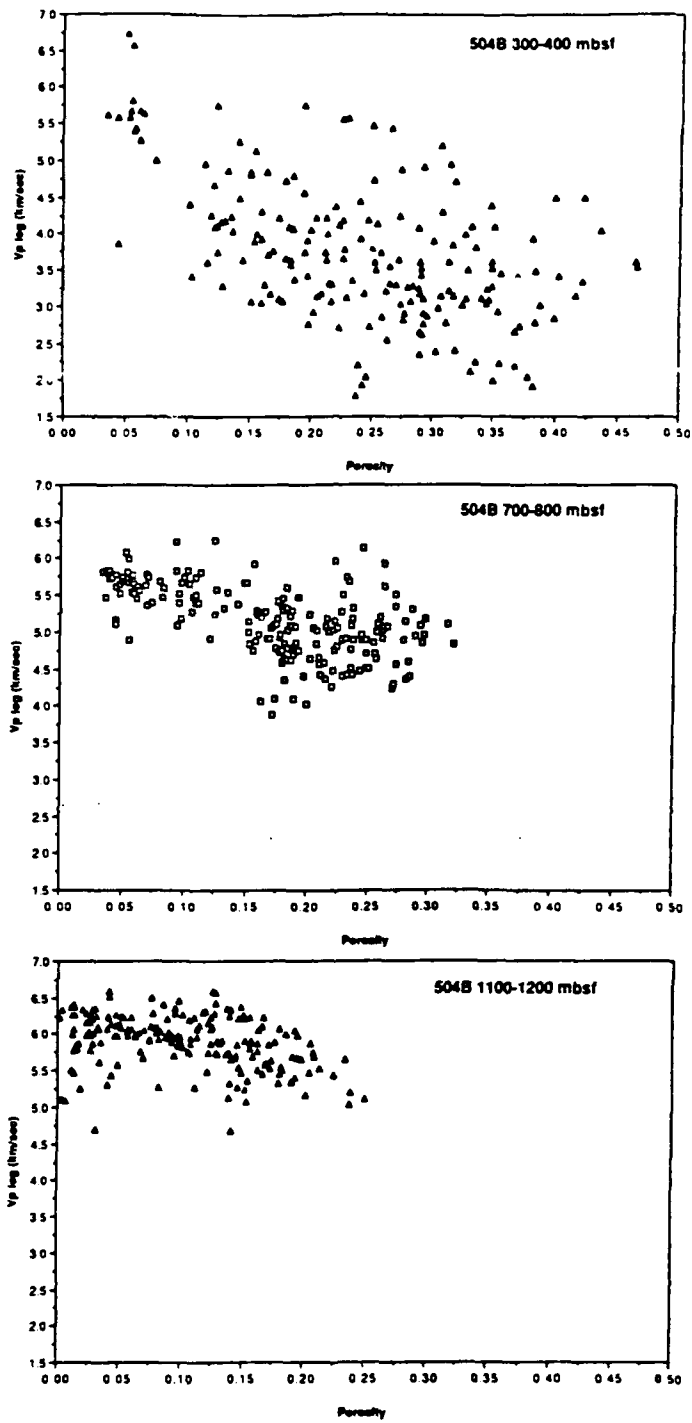
Figure 2: Velocity-Porosity distributions at Hole 504B from downhole logs. The decrease in slope downhole indicates an increase in the mean aspect ratio (see Figure 1). Basement begins at 300 m below seafloor (mbsf).

must have been subsequent crack filling and reduction in the mean aspect ratio within the upper few hundred meters, precisely what we would have predicted if alteration products seal narrow voids first. A paper describing this work will be submitted in summer 1990.

Through appeal to rock physics, seismic wave propagation, downhole logging, and hydrothermal geochemistry, we are now expanding the porosity study into a multidisciplinary investigation (funded by ONR) of how geological processes affect seismic structure of the shallow crust.

Publications Supported by This Project

Berge, P. A., and G. J. Fryer, 1989. *In situ* measurement of anisotropy in marine sediments [Abstract], *Seismological Research Letters,* **60,** 16.

Berge, P. A., and G. J. Fryer, 1989. *In situ* measurement of anisotropy in marine sediments using multicomponent data [Abstract], *SEG Research Workshop on Recording and Processing Vector Wavefields, Snowbird, Utah, August 13-17, 1989, Technical Abstracts, 71.*

Berge, P. A., S. Mallick, G. J. Fryer, N. Barstow, J. A. Carter, G. H. Sutton, and J. Ewing, *In situ* measurement of transverse isotropy in shallow-water marine sediments, submitted to *Geophs. J. Int.* [Reproduced here as Appendix.]

Fryer, G. J., and R. H. Wilkens, 1989. Making sense of seismic velocities in shallow oceanic crust [Abstract], *Seismological Research Letters,* **60,** 16.

Appendix

PREPRINT
**In situ measurement of transverse isotropy
in shallow-water marine sediments**

by
Patricia A. Berge, Subhashis Mallick, Gerard J. Fryer, Noël Barstow,
Jerry A. Carter, George H. Sutton, and John Ewing

In Situ measurement of transverse isotropy

in shallow–water marine sediments

Patricia A. Berge,[1] Subhashis Mallick,[1] Gerard J. Fryer,[1] Noël Barstow,[2] Jerry A. Carter,[2] George H. Sutton [2] and John I. Ewing [3]

[1] *Hawaii Institute of Geophysics, 2525 Correa Road, Honolulu, HI 96822, USA*

[2] *Rondout Associates, Incorporated, P.O. Box 224, Stone Ridge, NY 12484, USA*

[3] *Woods Hole Oceanographic Institution, Woods Hole, MA 02543, USA*

SUMMARY

The interleaving of parallel isotropic lamellae of contrasting mineralogical composition makes almost all marine sediments anisotropic, the form of anisotropy being transverse isotropy with a vertical axis of symmetry. Yet conventional marine seismic experiments cannot quantify the anisotropy because they do not record unconverted shear waves. In 1986, Rondout Associates, Inc. (RAI) and Woods Hole Oceanographic Institution (WHOI) recorded direct shear waves in anisotropic shallow marine sediments by using a newly developed ocean-bottom shear source and a multi-component on-bottom receiver. The seismic experiment was conducted in 21-m-deep water about 10 km east of the New Jersey coast. In this paper, we describe the anisotropy in the top 50 m of marine sediments beneath two of the RAI/WHOI refraction profiles. We use an anisotropic reflectivity program to produce synthetic seismograms to estimate the five independent elastic stiffnesses necessary for describing the transverse isotropy. Our synthetics fit the vertical and two horizontal components of the data for both profiles. The two intersecting refraction profiles are 150 m and 200 m long. These profiles are not long enough to constrain compressional wave velocities and anisotropy, but are quite adequate to find the shear wave anisotropy. A nearby drill hole showed that the sediments are interbedded silty clays, clays, and sands. The data require low shear velocities (< 400 m/s) and low Q_s (< 100) in about the top 30 m of the sediments. In the top 10 m of the sediments, silty clay exhibits ~ 12–15% anisotropy for shear waves.

Key words: seismic anisotropy, transverse isotropy, marine sediments, shear waves.

1 INTRODUCTION

Conventional marine seismic studies assume an isotropic velocity structure for marine sediments. Yet marine sediment cores routinely show anisotropy (Bachman 1979, 1983; Carlson, Schaftenaar & Moore 1984). Although highly anisotropic minerals such as calcite make up typical sediments, within each sedimentary microlayer these minerals orient randomly, making individual microlayers isotropic. Anisotropy of marine sediments results primarily from bedding, the interleaving of thin isotropic layers (Carlson *et al.* 1984). Any medium composed of different isotropic layers that are much thinner than a seismic wavelength is anisotropic. This lamellate medium will exhibit transverse isotropy with an axis of symmetry orthogonal to the layering (Postma 1955; Backus 1962).

To completely describe the compressional and shear wave velocities of seismic waves travelling in an arbitrary direction through a transversely isotropic (TI) medium, five independent elastic parameters are required (Love 1920). Determining all five parameters necessitates recording compressional waves, and shear waves in two directions. Conventional marine seismic experiments may detect indications of anisotropy, such as mismatches between models derived from reflection and refraction studies (Davis & Clowes 1986) or discrepancies between seismic models and drill hole data (Banik 1984). But quantifying the anisotropy completely (*i.e.* determining all five parameters) is impossible unless unconverted shear waves are recorded.

Recently, it has become technologically feasible for marine experiments to record unconverted shear waves by using multi-component ocean-bottom receivers and newly developed ocean-bottom sources (Sutton *et al.* 1987; Carter *et al.* 1987; Dorman *et al.* 1986, 1987; Akal, Schmidt & Curzi 1986; Gehrmann, Gimpel & Theilen 1984). In this paper, we describe the successful *in situ* measurement of transverse isotropy in shallow marine sediments, using an ocean-bottom shear source. We have estimated all five elastic stiffnesses for the TI sediments. This work has significant implications for the mineralogy of the sediments and also for the design of future experiments to quantify anisotropy.

2 BACKGROUND

2.1 Experiment

In 1986, Rondout Associates, Inc. (RAI) and Woods Hole Oceanographic Institution (WHOI) used an ocean-bottom source and an ocean-bottom sensor to investigate the detailed seismic velocity and attenuation structure of shallow marine sediments off the coast of New Jersey (Sutton *et al.* 1987; Carter *et al.* 1987). The ocean-bottom shear wave source sled developed by WHOI is shown in Fig. 1. The sled held two horizontally mounted 10-cubic-inch airguns that fired in opposing directions (port and starboard). Runners on the sled bottom transmitted SH energy into the sediments when the guns were fired individually. The airgun blasts produced abundant P-SV energy. For the shear waves, the dominant frequency was about 10 Hz, while compressional waves had dominant frequencies of about 20–30 Hz recorded on the vertical component geophone. Similar sources have been used previously by Akal *et al.* (1986) and Gehrmann *et al.* (1984).

For the ocean-bottom sensor, three orthogonal geophones and a hydrophone were all mounted on a receiver toboggan, which was deployed at different distances from the source sled, to record high-resolution refraction profiles. Misalignment of the receiver toboggan could be corrected by rotating the horizontal component data to the azimuth at which the first arrival showed the smallest transverse horizontal amplitude. Occasional misalignment of the source sled decreased the amplitude of the SH waves generated, without otherwise affecting the results (Carter *et al.* 1987).

Summing the data recorded from the two oppositely directed airguns emphasized the P and SV waves on the vertical and radial horizontal components. This procedure cancelled SH waves on the transverse horizontal component. Similarly, differencing the data from the port and starboard airguns emphasized the SH waves on the transverse horizontal component, while cancelling the P and SV waves on the vertical and radial horizontal components. In this manner, record sections for vertical, radial horizontal, and transverse horizontal motion were constructed (Sutton *et al.* 1987; Carter *et al.* 1987).

2.2 Setting

The two profiles we discuss in the present paper were recorded in 21-m-deep water near the Atlantic Margin Coring Project (AMCOR) hole number 6011 (Fig. 2). The longer profile is about 200 m long, with an average receiver spacing of about 8 m. The shorter

profile is about 150 m long, with the same average receiver spacing. The two profiles are unreversed, but do intersect. Some lateral heterogeneity is probably present in the shallow marine sediments beneath the two profiles, but the bathymetry is fairly uniform (Fig. 2) and the shallowest sediments do not dip significantly (Hathaway et al. 1976). Drill cores collected at the 6011 site during the U.S. Geological Survey's AMCOR project (Hathaway et al. 1976) show that the sediments are interbedded silty clays, clays, and sands (Fig. 3). Because the cores were severely disturbed, sediment interface depths determined from the drilling results are accurate to ±9 m, the length of a core (Richards 1978). Although longer wavelength energy may penetrate slightly deeper, refracted rays for the 200-m-long profile probably sample no more than the top 50 meters of these sediments. ~ 10 m of silty clay overlying ~ 40 m of sand. We expect the silty clay to be TI because of compositional layering at the grain scale (Carlson et al., 1984).

Geotechnical studies of the AMCOR 6011 drill cores estimated the porosity and density of the sediments (Richards 1978). Most of the cores from this hole were severely disturbed, limiting the accuracy of the geotechnical studies. Porosity was 0.57 at 8.8 m depth below the sea floor, with a water content of 47% of the dry weight of the sediments. Shipboard measurements using the Lehigh University nuclear densitometer provided density estimates of 2300 kg/m^3 at 8.9 m depth below the sea floor, 2100 kg/m^3 at 32.4 m depth, and 2140 kg/m^3 at 61.1 m. On-shore density measurements by the Marine Geotechnical Laboratory of Lehigh University resulted in low values of 1690 kg/m^3 at 8.8 m depth, because some air was trapped in the measurement container. The shipboard density estimates were considered to be more reliable than the on-shore measurements (Richards 1978).

3 DATA

Unfiltered vertical, horizontal, and pressure component record sections from the long profile recorded near the AMCOR 6011 site are shown in Fig. 4(a–d). Direct-wave arrivals recorded on the hydrophone (Fig. 4d) were used to determine the distances between the source and receiver sleds, with an uncertainty of about ±2 m. The hydrophone data were not used in synthetic seismogram modeling. The radial horizontal (X) component record section (Fig. 4a) was constructed by summing the signals from the port and starboard airguns.

The transverse (Y) component record section (Fig. 4b) was produced by differencing the two signals. For the vertical (Z) component (Fig. 4c) and the pressure component (Fig. 4d), the airgun signals were not summed because the record sections from the individual guns already had a high signal-to-noise ratio. Further enhancement was unnecessary.

Similar record sections for the short profile are presented in Fig. 5(a–d). The absence of large P-arrivals on most of the transverse component record sections (Fig. 4b, 5b) for the two profiles shows that the receivers were not significantly misaligned in the X-Y plane. Therefore none of these data have been rotated.

The Z component record section for the long profile (Fig. 4c) shows small amplitude P waves as first arrivals, followed by larger amplitude refracted SV waves a few tenths of a second later. The SV waves merge into SV waves from deeper layers and large amplitude Stoneley waves, which are the most prominent phases on the Z record section.

On the X component record section for the long profile (Fig. 4a), the same three sets of arrivals appear. Here the P waves have larger amplitudes than on the vertical component, and the later emergent SV waves and Stoneley waves are slightly smaller.

The Y component record section for the long profile (Fig. 4b) differs from the other components in that most traces show no P arrival. On the traces at extremely short ranges, the apparent first arrival is actually an artifact resulting from an approximately $30°$ misalignment of the receiver sled. If the source and receiver were perfectly aligned, the transverse horizontal component would show only Love waves and SH waves, but no P waves. This artifact can be filtered out of the data. Misalignment angles for the Y component receiver were smaller than $15°$ for all ranges beyond 34 m. Therefore the first arrivals on most of the Y component traces are large amplitude SH waves followed by Love waves, as expected.

Comparing the X and Y data (Fig. 4a, b), we note that the group velocity of the SH and Love waves on the Y component appears to be higher than the group velocity of the SV and Stoneley waves on the X component. This is most evident for ranges beyond about 100 m, where the X component data show a gap of about 0.2 s duration between the earliest SV refractions and the onset of the SV refraction arrivals from deeper layers, which

merge into the Stoneley waves. On the Y component, the SH and Love waves are already present at the time of the X component gap.

Record sections for the short profile (Fig. 5, a-d) show the same arrivals as the long profile data (Fig. 4, a-d). A comparison of the data from the two profiles shows that on the X components (Fig. 4a, Fig. 5a), P arrivals and SV arrivals at short ranges are slightly larger for the short profile than for the long profile and no traces for the short profile Y component (Fig. 5b) show the spurious P arrivals seen at short ranges on the long profile (Fig. 4b). None of these differences are significant. We note, however, that for the X and Z components, the earliest SV arrivals are a few hundredths of a second earlier on the short profile than they are on the long profile. Otherwise, travel times, frequencies, and amplitudes on the record sections for the two profiles are comparable. This implies that some lateral heterogeneity may be present in the deeper layers sampled by the earliest SV arrivals, but that in shallower layers the sediments underlying the two profiles are the same. Therefore we do not expect much lateral heterogeneity to complicate our modeling. The similarity of the two profiles, which were shot at two different azimuths (Fig. 2), also rules out the possibility of azimuthal anisotropy in the sediments. However, the fact that the group velocities of the SH and Love waves on the Y components of the two profiles appear to be higher than the group velocities of the SV and Stoneley waves on the X and Z components of both profiles suggests that the sediments are TI.

4 ISOTROPIC MODELS

To investigate the details of the seismic velocity structure near the AMCOR 6011 site, RAI seismologists modeled the horizontal and vertical component data from the 200-m-long profile using full-waveform synthetic seismograms based on the "locked mode" technique developed by Harvey (1981). Fig. 6(a-c) compares RAI's best-fitting synthetic seismograms with data from the vertical and the two horizontal components for the long profile (Sutton et al. 1987). Because the group velocities for the SV/Stoneley waves and the SH/Love waves differ, all three components of the data could not be fit using a single model. The model for the X and Z component data required lower shear velocities than the model for the Y component data (Fig. 7). The RAI model which produced the synthetic seismograms

(Fig. 6a, c) with the best fit to the X and Z component data used a 15-m-thick isotropic layer with shear velocities of 175–310 m/s, overlying an isotropic layer with shear velocities of 340–396 m/s. This would correspond to 15 m of silty clay overlying higher velocity sand, in Fig. 3. The Y component data, however, were best fit (Fig. 6b) using a model with shear velocities of 184 to 325 m/s in the top 15 m layer. Sutton *et al.* (1987) concluded that the shallow marine sediments near the AMCOR 6011 site are anisotropic.

5 ANISOTROPIC REFLECTIVITY MODELING

We expect silty clay to exhibit transverse isotropy with a vertical axis of symmetry. Only vertically travelling and horizontally travelling P and SV waves are pure-mode in such a medium. At other attitudes, particle motion is neither parallel to nor perpendicular to the direction of propagation. Hence, the waves are quasi-P (qP) and quasi-SV (qSV) in the TI medium (Auld 1973). In a TI medium, because of axial symmetry the 21 elastic stiffnesses of general anisotropy reduce to five: $C_{11}, C_{13}, C_{33}, C_{44}$, and C_{66} (Love 1920). With this symmetry, the velocity of a horizontally travelling SH wave is $\sqrt{C_{66}/\rho}$ where ρ is density; the velocity of a horizontally travelling SV wave is $\sqrt{C_{44}/\rho}$ (Stoneley 1949). The velocity of a Love wave in a TI medium depends on C_{44} and C_{66} (Stoneley 1949; Anderson 1961). The velocities of Rayleigh and Stoneley waves depend on C_{11}, C_{13}, C_{33}, and C_{44}, but not on C_{66} (Anderson 1961).

In a TI medium, energy considerations require that the elastic stiffnesses meet certain conditions:

$$C_{11} \geq C_{66} \geq 0 \tag{1}$$

$$C_{33} \geq 0 \tag{2}$$

$$C_{44} \geq 0 \tag{3}$$

$$C_{13}'^2 \leq C_{33}(C_{11} - C_{66}) \tag{4}$$

(Postma 1955; Auld 1973; Backus 1962). When the TI medium is comprised of thin isotropic layers, we have the additional constraints:

$$C_{33} > C_{13} \tag{5}$$

$$C_{33} > \frac{4}{3}C_{44} \tag{6}$$

$$C_{66} \geq C_{44} \tag{7}$$

(Backus 1962). Considering earlier versions of the RAI models shown in Fig. 7 for the X-Z and Y components, or Stoneley waves and Love waves, respectively, led us to think that the lower shear velocities for the top 15 m of sediments in the X and Z component isotropic model were related to C_{44}, while the higher shear velocities for the top of the Y component model were probably related to C_{66}. We used these ideas and the constraints given by inequalities (1)–(7) to combine preliminary versions of the two isotropic RAI models to construct a TI model, with five independent elastic stiffnesses for the 10-m-thick silty clay layer seen in the drill cores (Fig. 3). Deeper layers in our starting model were assumed to be isotropic. In our modeling, we used a density of 2100 kg/m^3 for the sediments.

For the long and short profile data (Fig. 4a–d, Fig. 5a–d), we expect the shear wavelengths to be approximately 15–30 m, at the dominant frequency of about 10 Hz. For the compressional waves, with dominant frequencies of about 20–30 Hz on the vertical component geophone, the wavelengths are > 50 m. (The hydrophone had higher frequencies, up to about 60 Hz, but we did not use the pressure component data in our modeling). Since the long profile is at most four qP wavelengths long, the two moduli C_{11} and C_{33}, which

determine compressional wave velocities. will be more poorly resolved than C_{44} and C_{66}. Proper constraint of C_{11} and C_{33} for the TI sediments would require much longer profiles.

Direct water-wave arrivals and reflected and refracted compressional waves from the 10 m boundary have travel times that differ by only a few milliseconds for ranges out to 200 m. The amplitudes of qP waves are much smaller than shear wave and interface wave amplitudes because the impedance contrasts and velocity gradients in the shallow sediments are much smaller for qP waves. In our modeling we use an estimate of C_{11} derived by raytracing for travel times of the first arrivals on the long profile vertical and pressure component data (Sutton *et al.* 1987), and we assume $C_{33} = C_{11}$. We can use synthetic seismogram modeling to fit the shear waves and interface waves, and therefore obtain estimates of the other three elastic stiffnesses. The long and short profile data, however. cannot constrain C_{11} and C_{33}. We therefore do not attempt to fit the compressional waves with our synthetic seismogram modeling.

5.1 Sources and filtering

To generate the synthetic seismograms, we assumed fairly simple sources. Plots of the frequency spectra of the data in Fig. 8(a–c) show that the airgun explosions recorded on the geophones produced energy in a narrow band from about 4 to 20 or 30 Hz. peaking near 10 Hz. and dropping off very steeply outside this band. The higher frequency energy corresponds to early qP arrivals. Shear waves and interface waves had frequencies near 10 Hz. We used a 4–25 Hz bandpass filter convolved with a point-source in the Y direction to simulate the port minus starboard shots that generated the transverse horizontal (Y) component energy. For the X and Z components. we used the same 4–25 Hz filter convolved with an explosion source.

We filtered the data with the same 4–25 Hz filter that was used for the synthetic seismograms. The filter removed the early artifact from the first few traces of the long profile Y component and slightly decreased qP amplitudes on the X and Z components. without otherwise significantly changing the data.

5.2 Synthetic seismograms

For each profile, we used the code ANIVEC^{TM} [†] running on a Cray supercomputer to produce synthetic seismograms to match all components of the data with a single model. ANIVEC^{TM} uses the Kennett imbedding algorithm (Kennett 1983) and two wavenumber-to-distance transformations to construct synthetic seismograms for a stratified medium with arbitrary anisotropy. A description of the algorithm can be found in Mallick & Frazer (1988, 1990). For the modeling described here the program was run in its single wavenumber transformation mode. (Since TI structures are azimuthally isotropic, the second transformation was not required).

We present here final synthetics obtained after iterative adjustment of the models. As usual in reflectivity computations, homogeneous layers much thinner than a wavelength were used to approximate gradients in the elastic stiffnesses. The final TI model (Table 1, Fig. 9) and synthetics (Fig. 11, a–c) for the long profile are discussed below, followed by the TI model (Table 2, Fig. 10) and synthetics (Fig. 12, a–c) for the short profile.

Long Profile

The X and Z component synthetic seismograms match all significant phases in the data for traces farther than one shear wavelength ($\sim$ 15–30 m) from the source (Fig. 11a, c). Closer to the source, the reflectivity program computes incorrect seismograms because of non-linear effects. A low value for C_{44} in the top 10 m of the sediments in our model (Table 1, Fig. 9), followed by a gradient and higher C_{44} in the deeper part of the model, produce two sets of large amplitude qSV arrivals which merge into smaller amplitude Stoneley waves. The low frequency ringing in the synthetics at short ranges is an artifact caused by using steep filter slopes. We have not attempted to fit the qP arrivals, but the arrival times and amplitudes in the X and Z component synthetics match the data fairly well for qP. We have used a constant shear wave quality factor of $Q_s = 15$ in the top 10 m of the sediments so that the amplitudes of the synthetic seismograms decrease correctly with distance from the source. The deeper part of the model has $Q_s = 60$. The compressional wave quality factor used was $Q_p \approx \infty$. Detailed modeling of the attenuation is beyond the scope of this paper.

[†] ANIVEC^{TM} is a trademark of Geo-Pacific Corporation.

Our synthetic seismograms match the travel times and amplitudes of the important phases in the X and Z component data (Fig. 11a, c), but do not perfectly fit small details of the data. We have not matched the high frequency ringing of the later qSV arrivals in the data, and in our synthetics the second to fourth cycles of the earliest qSV arrivals are smaller, instead of larger, than the first qSV cycles. Our model matches gross features, but small inhomogeneities and details with scale-lengths smaller than about one-quarter of a shear wavelength (15–30 m) cannot be resolved. If we had used a narrower frequency bandwidth for the data and synthetics (e.g. Fig. 6), we would have produced synthetics that looked more like the data since we then would not have had to contend with the frequency-dependence of velocities and attenuation in the real earth. But instead we have produced synthetics that represent the average structure over all frequencies for which we have significant shear and interface wave energy (Fig. 8). The resulting modeling is not unique, yet it can inform us about the properties of these marine sediments.

Our synthetic seismograms for the Y component (Fig. 11b) show small amplitude refracted SH waves as the first arrivals. These are followed by larger amplitude SH arrivals from the shallowest part of the model, merging into Love waves, as in the data. Again the low frequency ringing in the synthetics at short ranges is caused by steep filter slopes. The Y component data require a gradient in C_{66} at the top of the model, and $C_{66} > C_{44}$ for the top 10 m of the sediments (Table 1).

The relative amplitudes and the arrival times of the phases in the Y component synthetics (Fig. 11b) match the data, except that the large amplitude SH wavelet has a simpler shape in the synthetics than in the data. Possibly a more complicated source wavelet would produce a better fit for the Y component. The isotropic RAI models for Fig. 6 used a source wavelet centered at 10 Hz, having a long rise time (Carter et al., 1987). That source would have removed the higher frequencies from our synthetics, so we did not choose to use it.

Like the X and Z component data, the Y component data required a low value of Q_s throughout the model. We used $Q_s = 60$.

Short Profile

The model for the short profile synthetic seismograms (Table 2, Fig. 10) differs from the long profile model (Table 1, Fig. 9) only in that the 5-m-thick gradient layer immediately below the top 10 m of sediments is not present. For the short profile X and Z component data (Fig. 12a, c), the same phases are present as were seen in the long profile data (Fig. 11a, c). The only significant difference between the data from the two profiles is that the earliest qSV arrivals, refracted arrivals from below the top 10 m of sediments, have shorter travel times on the short profile than on the long profile. The time difference is only a few hundredths of a second. This difference probably represents lateral velocity heterogeneity in the deeper sediments beneath the two profiles. Our synthetics for the X and Z components of the short profile (Fig. 12a, c) are very similar to those for the long profile, except that now the first qSV arrivals are slightly earlier than on the long profile.

For the Y component, the short profile data again require $C_{66} > C_{44}$ and a gradient in the top 10 m of the sediments. We have used the same values of Q_s in the model in Table 2 for the short profile as we used in Table 1 for the long profile.

6 DISCUSSION

In both profiles, qP waves and Stoneley waves help to constrain C_{11}, C_{13}, C_{33}, and C_{44}. In our modeling, C_{44} is better constrained than C_{66}, since C_{66} only affects the Y component data. A comparison of the data to the synthetics (Fig. 11a, c; Fig. 12a, c) shows that we are using correct values of C_{44} since we obtain correct arrival times for the qSV waves on the vertical component (Fig. 11c, Fig. 12c) of both profiles as well as on the X components (Fig. 11a, 12a).

6.1 Constraints on C_{13}

One of the frustrations of working with TI media is the poor control of the modulus C_{13}, which is potentially of great importance to seismic interpretation (Bachman 1983). In this study, the recording of shallow and deep penetrating shear waves and the energy partition between these arrivals allows us to put useful constraints on C_{13}. Although the parameter C_{13} does not affect the velocities of qP and qSV waves propagating parallel to or perpendicular to the vertical axis of symmetry, C_{13} profoundly affects these velocities for waves travelling in all other directions. Wavefronts in an anisotropic medium are aspherical, but

not necessarily ellipsoidal, in general. The qSV wavefronts can even have cusps, depending on the value of C_{13} (Helbig 1966). We illustrate the effect of C_{13} on wavefront shapes in Fig. 13. All other stiffnesses are held constant in this figure, while different values of C_{13} change the shapes of the wavefronts (velocity surfaces) for qP and qSV waves. Moving clockwise from the top, along a qSV slowness or velocity surface in this figure, is equivalent to moving to closer ranges towards the source, along a refraction profile. Cusps in the velocity surface can have the same effect as velocity inversions have in isotropic structures, turning rays away from the earth's surface and producing shadow zones. The parameter C_{13} greatly affects the partitioning of the energy between the refracted qSV waves and the Stoneley waves in our X and Z component data, because the angle of incidence determines whether energy propagates as head waves or as evanescent waves, and C_{13} determines the velocities for different angles of incidence. We fit the data by using the values of C_{13} shown in Tables 1 and 2 for the top 10 m of the sediments. Changes of even a few percent or the introduction of a slight gradient in C_{13} produced synthetic seismograms in which the relative amplitudes of the qSV and Stoneley waves no longer matched the data (Fig. 14). Note how the amplitudes of the latest qSV arrivals die off too quickly in Fig. 14, even though Q_s has not been decreased from the values used in Fig. 11(a, c). (The Y component is not displayed in Fig. 14 since C_{13} does not affect SH or Love wave velocities). We believe our modeling (Fig. 11,12) constrains C_{13} in the top 10 m quite well.

6.2 Anisotropy resulting from thin layering

In our models (Tables 1, 2), $C_{33} > C_{13}$ and $C_{66} > C_{44}$ for the top 10 m of the sediments. This is consistent with inequalities (5) and (7), which constrain media in which transverse isotropy results from thin isotropic layers. Our models in Tables 1 and 2 show that thin layering could be the cause of the anisotropy in the top 10 m of the sediments. This 10-m anisotropic layer at the top of the models agrees with the drill core data, since silty clay is expected to exhibit transverse isotropy (Carlson *et al.* 1984).

The slowness surfaces and velocity surfaces (wavefront shapes) for the top 10 m of the model in Table 1 are shown in Fig. 15(a, b). For the deeper, isotropic layers of the model, slowness and velocity surfaces are spherical. Helbig (1966) has shown that for a TI medium

with a vertical axis of symmetry in which thin isotropic layers cause the anisotropy, the qSV wavefront may have cusps at intermediate angles but may not have cusps in the vertical or horizontal directions. Our model has cusps at $45°$ (Fig. 15b). Although the anisotropy could have a different cause, these intermediate angle cusps are not inconsistent with our assertion that the anisotropy in the silty clay may be caused by the interleaving of parallel laminae of contrasting mineralogical makeup.

7 CONCLUSIONS

Seismic energy adequately samples about the top 30 m of the sediments with a resolution of about one shear wavelength, 15–30 m, in this study. We tried models with anisotropic layers thicker than 10 m, with velocity reversals in the top layers, and with density gradients near the sea floor, but none of those models produced better-fitting synthetics than those produced by the models in Tables 1 and 2. Our final best-fitting models do not exactly match the shear velocity structures in the final RAI isotropic models in Fig. 7, but agree within the limits of resolution of this study. The data require low near-surface shear velocities (< 400 m/s) and low values of Q_s (< 100). In this our models agree with the isotropic modeling results. We used the simplest models that produced a good fit to the data and agreed with the drill core results. Our models give the average structure over frequencies of 4–25 Hz for depths to 1 or 2 shear wavelengths in the sediments near the AMCOR 6011 drill site. Using the formula:

$$k = \frac{V_{max} - V_{min}}{V_{mean}} \tag{8}$$

(Birch 1960, 1961; Babuška 1984), we find that the amount of shear wave anisotropy in the top 10 m of these sediments is about 12–15 %.

The fit of the synthetic seismograms to the data (Fig. 11a–c, Fig. 12a–c) justifies our conclusion that the shallow sediments near AMCOR hole 6011 are, indeed, anisotropic. We have quantified the anisotropy by estimating the values of all five elastic stiffnesses necessary to describe a TI medium.

Ignoring anisotropy in marine data may lead to systematic errors in interpretation, including overestimates of depth and errors in Poisson's ratio (Fryer, Miller & Berge 1990).

Moreover, the anisotropy can be exploited to yield information about the geologic structure. By assuming that the anisotropy results from interlayering of two or three isotropic components, such as siliceous and calcareous minerals expected in silty clay, we can use the five elastic stiffnesses obtained from our synthetic seismogram modeling to estimate the bulk and shear moduli of the isotropic components (Backus 1962; Helbig 1981). The five elastic stiffnesses yield at least two Poisson's ratios for the silty clay, which can tell us something about porosity and pore geometry. Because it constrains mineralogy and porosity, anisotropy can actually provide information about structures whose scale is finer than a seismic wavelength (Helbig 1981).

We have used a TI model, rather than more general anisotropy with some azimuthal variation, because vertical cracks in the top few tens of meters of marine sediments, and ripple marks or dunes on the sea floor, are probably too small to produce significant azimuthal anisotropy. The two intersecting profiles, recorded at two different azimuths, showed no evidence of azimuthal anisotropy. Our TI model is geologically reasonable and satisfies the observations. These data are inadequate for measuring azimuthal variations. A complete experiment would require measurements over a full range of azimuths. Strong tidal currents would make that a formidable task at this site.

Future experiments to measure anisotropy in marine sediments and the oceanic crust must use on-bottom shear sources and multi-component on-bottom receivers. Longer profiles than the one we describe should be recorded, to constrain C_{11} and C_{33}. But the shot spacing must be kept fine enough to sample on the scale of shear wavelengths. These requirements could be satisfied by using closely spaced instruments near the source, but then extending receivers far from the source, with wider spacing. In this way, the expense of a vertical seismic profile could be avoided, as well as the attendant problems of being unable to measure C_{13} adequately because of lateral heterogeneities and too few horizontal raypaths. Our results demonstrate that five elastic stiffnesses can realistically be estimated using high-quality marine data recorded with on-bottom sources and receivers. The success of this investigation should encourage the development of deep-water shear sources to investigate anisotropy in pelagic sediments and in the oceanic crust.

ACKNOWLEDGMENTS

REFERENCES

Akal, T., Schmidt. H. & Curzi, P., 1986. The use of Love waves to determine the geoacoustic properties of marine sediments, in *Ocean Seismo-Acoustics, Low-Frequency Underwater Acoustics, NATO Conference Series IV: Marine Sciences*, **16**, pp. 841-852, eds. Akal., T. & Berkson. J. M., Plenum Press, New York.

Anderson, D. L., 1961. Elastic wave propagation in layered anisotropic media, *J. Geophys. Res.*, **66**, 2953-2963.

Auld, B. A., 1973. *Acoustic Fields and Waves in Solids, Vol. 1 & 2*, John Wiley & Sons, New York.

Babuška, V., 1984. *P*-wave velocity anisotropy in crystalline rocks, *Geophys. J. R. astr. Soc.*, **76**, 113-119.

Bachman, R. T., 1979. Acoustic anisotropy in marine sediments and sedimentary rocks, *J. Geophys. Res.*, **84**, 7661-7663.

Bachman, R. T., 1983. Elastic anisotropy in marine sedimentary rocks, *J. Geophys. Res.*, **88**, 539-545.

Backus, G. E., 1962. Long-wave elastic anisotropy produced by horizontal layering, *J. Geophys. Res.*, **67**, 4427-4440.

Banik, N. C., 1984. Velocity anisotropy of shales and depth estimation in the North Sea basin, *Geophysics*, **49**, 1411-1419.

Birch, F., 1960. The velocity of compressional waves in rocks to 10 kilobars: Part 1, *J. Geophys. Res.*, **65**, 1083-1102.

Birch, F., 1961. The velocity of compressional waves in rocks to 10 kilobars: Part 2, *J. Geophys. Res.*, **66**, 2199-2224.

Carlson, R. L., Schaftenaar, C. H. & Moore, R. P., 1984. Causes of compressional-wave anisotropy in carbonate-bearing, deep-sea sediments, *Geophysics*, **49**, 525-532.

Carter, J. A., Sutton, G. H., Barstow, N. & Ewing, J. I., 1987. Synthetic modeling of shear waves in shallow marine sediments, *Journal of the Acoustical Society of America*, **82**, suppl. 1, S112.

Davis, E. E. & Clowes, R. M., 1986. High velocities and seismic anisotropy in Pleistocene turbidites off Western Canada. *Geophys. J. R. Astron. Soc.*, **84**, 381–399.

Dorman, L. M., Hildebrand, J. A., Hammer, P. T. C., Sauter, A. W. & Schreiner, A. E., 1986. Seismic study of a seamount interior. *Eos. Trans. Am. Geophys. Union*, **67**, 1083.

Dorman, L. M., Hildebrand, J. A., Cornuelle, B. & Hammer, P. T. C., 1987. Seismic study of the interior of Jasper Seamount. *Eos, Trans. Am. Geophys. Union*, **68**, 1372.

Fryer, G. J., Miller, D. J. & Berge, P. A., 1990. Seismic anisotropy and age-dependent structure of the upper oceanic crust, in *The Evolution of Mid-Oceanic Ridges*, ed. Sinton, J. M., Am. Geophys. Union, Washington, D.C., in press.

Gehrmann, T., Gimpel, P. & Theilen, F., 1984. Marine shear wave profiling, *54th Annual International Meeting, Society of Exploration Geophysicists, Abstracts and Biographies*, 592–594.

Harvey, D. J., 1981. Seismogram synthesis using normal mode superposition: the locked mode approximation. *Geophys. J. R. Astron. Soc.*, **66**, 37–69.

Hathaway, J. C., Schlee, J. S., Poag, C. W., Valentine, P. C., Weed, E. G. A., Bothner, M. H., Kohout, F. A., Manheim, F. T., Schoen, R., Miller, R. E. & Schultz, D. M., 1976. Preliminary summary of the 1976 Atlantic Margin Coring Project of the US Geological Survey. US Department of the Interior Geological Survey. Open File Report No. 76-844.

Helbig, K., 1966. A graphical method for the construction of rays and travel times in spherically layered media. Part 2: Anisotropic case, theoretical considerations. *Bulletin of the Seismological Society of America*, **56**, 527–559.

Helbig, K., 1981. Systematic classification of layer-induced transverse isotropy. *Geophysical Prospecting*, **29**, 550–577.

Kennett, B. L. N., 1983. *Seismic Wave Propagation in Stratified Media*. Cambridge University Press, Cambridge.

Love, A. E. H., 1920. *A Treatise on the Mathematical Theory of Elasticity*. 3rd ed., Cam-

bridge University Press, Cambridge.

Mallick, S. & Frazer, L. N., 1988. Rapid computation of multioffset vertical seismic profile synthetic seismograms for layered media, *Geophysics*, **53**, 479-491.

Mallick, S. & Frazer, L. N., 1990. Computation of synthetic seismograms for stratified azimuthally anisotropic media, *J. Geophys. Res.*, in press.

Miller, D. J., 1987. Transverse isotropy: some consequences for travel time inversion and models of the oceanic crust, *MS thesis*, University of Hawaii.

Postma, G. W., 1955. Wave propagation in a stratified medium, *Geophysics*, **20**, 780-806.

Richards, A. F., 1978. Atlantic Margin Coring Project 1976. Preliminary report on shipboard and some laboratory geotechical data. US Department of the Interior Geological Survey. Open File Report No. 78-123.

Stoneley, R., 1949. The seismological implications of aelotropy in continental structure, *Monthly Notices of the Royal Astronomical Society, Geophysical Supplement*, **5**, 343-353.

Sutton, G. H., Ewing, J. I., Dubois, D. L., Barstow, N. & Carter, J. A., 1987. Shear velocity/attenuation models for shallow marine sediments: offshore New Jersey, *Eos, Trans. Am. Geophys. Union*, **68**, 354.

Table 1. TI model used to generate reflectivity synthetic seismograms for long profile (Figure 11), using $\rho = 2100$ kg/m^3.

C_{11}	C_{13}	C_{33}	C_{44}	C_{66}	depth[†]
		GPa			m
2.25	2.25	2.25	0.0	0.0	0.0–21.0
5.544	5.376	5.544	0.0526	0.0669	21.0–23.5
5.544	5.376	5.544	0.0526	0.0683	23.5–26.0
5.544	5.376	5.544	0.0526	0.0700	26.0–28.5
5.544	5.376	5.544	0.0526	0.0714	28.5–31.0
5.586	5.376	5.586	0.0792	0.0864	31.0–33.5
5.586	5.366	5.586	0.110	0.110	33.5–36.0
5.649	5.383	5.649	0.133	0.133	36.0–38.5
5.754	5.438	5.754	0.158	0.158	38.5–41.0
5.859	5.495	5.859	0.182	0.182	41.0–43.5
5.964	5.550	5.964	0.207	0.207	43.5–46.0
6.069	5.607	6.069	0.231	0.231	46.0–∞

[†] Source and receiver are below 21 m of seawater. All depths are in meters below sea level.

Table 2. TI model used to generate reflectivity synthetic seismograms for short profile (Figure 12), using $\rho = 2100$ kg/m^3.

C_{11}	C_{13}	C_{33}	C_{44}	C_{66}	depth[‡]
		GPa			m
2.25	2.25	2.25	0.0	0.0	0.0–21.0
5.544	5.376	5.544	0.0526	0.0669	21.0–23.5
5.544	5.376	5.544	0.0526	0.0683	23.5–26.0
5.544	5.376	5.544	0.0526	0.0700	26.0–28.5
5.544	5.376	5.544	0.0526	0.0714	28.5–31.0
5.649	5.383	5.649	0.133	0.133	31.0–33.5
5.754	5.438	5.754	0.158	0.158	33.5–36.0
5.859	5.495	5.859	0.182	0.182	36.0–38.5
5.964	5.550	5.964	0.207	0.207	38.5–41.0
6.069	5.607	6.069	0.231	0.231	41.0–∞

[‡] Source and receiver are below 21 m of seawater. All depths are in meters below sea level.
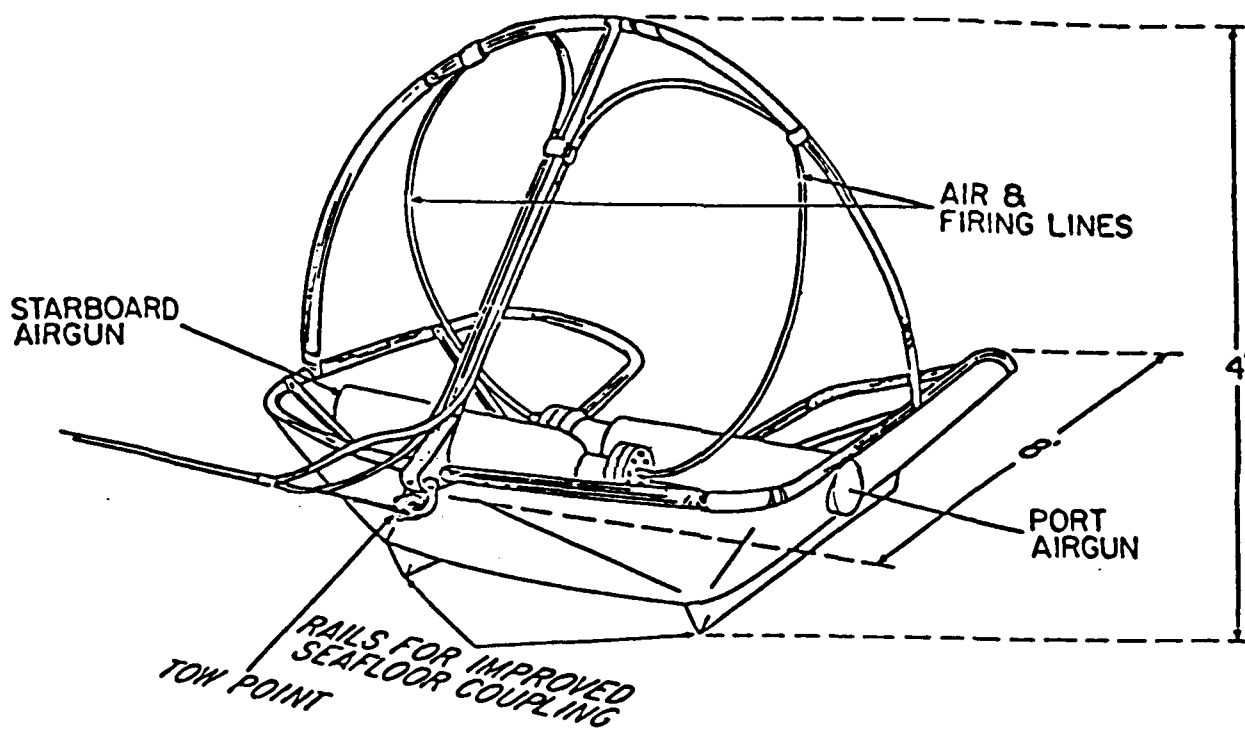
Figure 1: Woods Hole Oceanographic Institution shear wave source sled. Rails along the bottom of the sled couple *SH* wave energy into the sediments (Sutton *et al.*, 1987; Carter *et al.*, 1987).
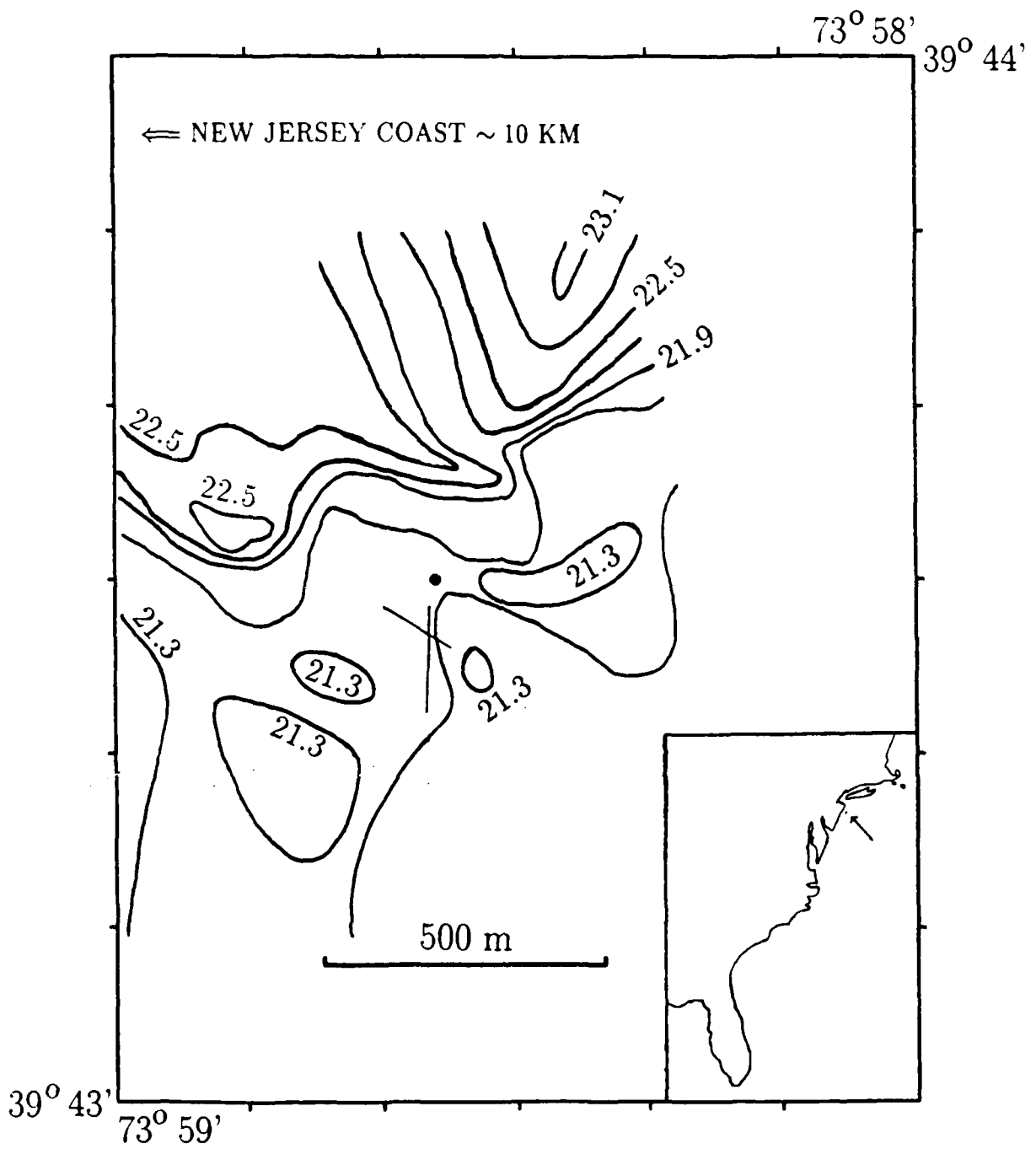
Figure 2: Location of the 1986 RAI/WHOI seismic experiment and nearby drill hole. Arrow and small dot in inset show map location. Large dot indicates drill site 6011 from the 1976 U. S. Geological Survey Atlantic Margin Coring (AMCOR) project (Hathaway *et al.* 1976). Straight lines indicate two intersecting seismic profiles recorded near AMCOR site 6011 in 1986 (Sutton *et al.* 1987; Carter *et al.* 1987). Curves show bathymetry in meters. Contour interval 0.305 m.

AMCOR HOLE 6011
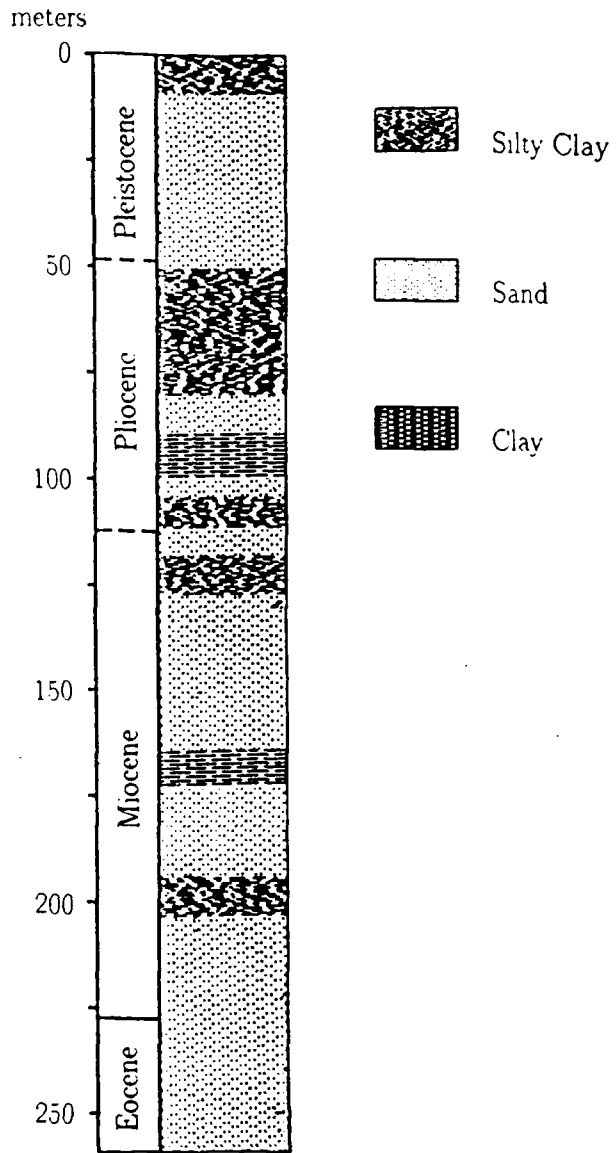
Figure 3: Stratigraphic section from AMCOR 6011 site (Hathaway *et al.*, 1976).

UNFILTERED DATA

(a) RADIAL (X) COMPONENT

(b) TRANSVERSE (Y) COMPONENT

DISTANCE (m)
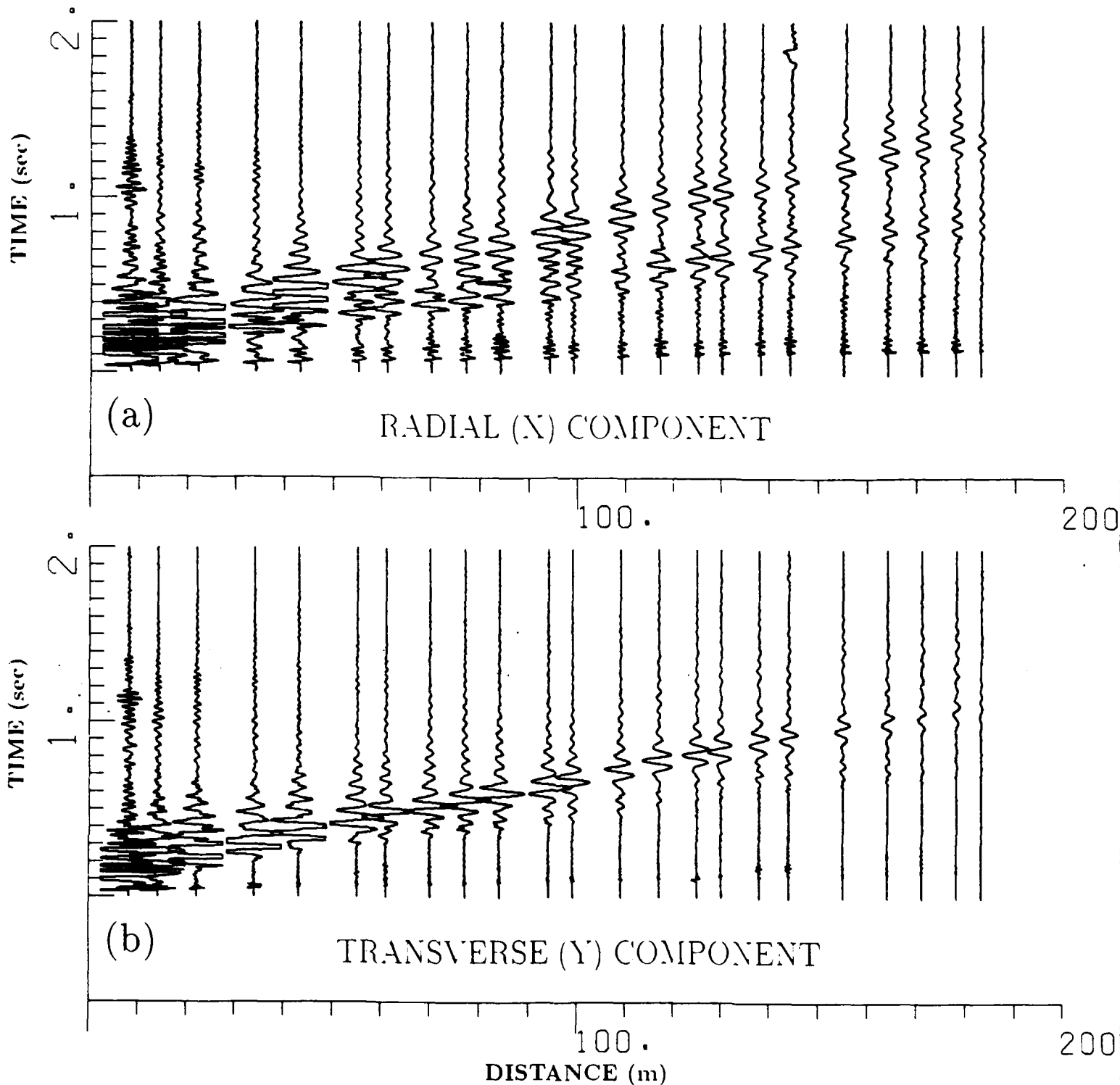
Figure 4: Record sections showing unfiltered data from the long seismic profile near the AMCOR 6011 site. North end of profile is plotted on the right; south end is to the left. Times (seconds) are unreduced; ranges are in meters. (a) Radial horizontal (X) component, from adding signals of port and starboard airguns. (b) Transverse horizontal (Y) component, by subtracting port from starboard airgun signals. (c) Vertical (Z) component, from starboard airgun signals. (d) Pressure (P) component, from starboard airgun signals recorded on hydrophone (Sutton *et al.* 1987; Carter *et al.* 1987).

UNFILTERED DATA

(c)

VERTICAL (Z) COMPONENT

(d)

PRESSURE (P) COMPONENT

DISTANCE (m)
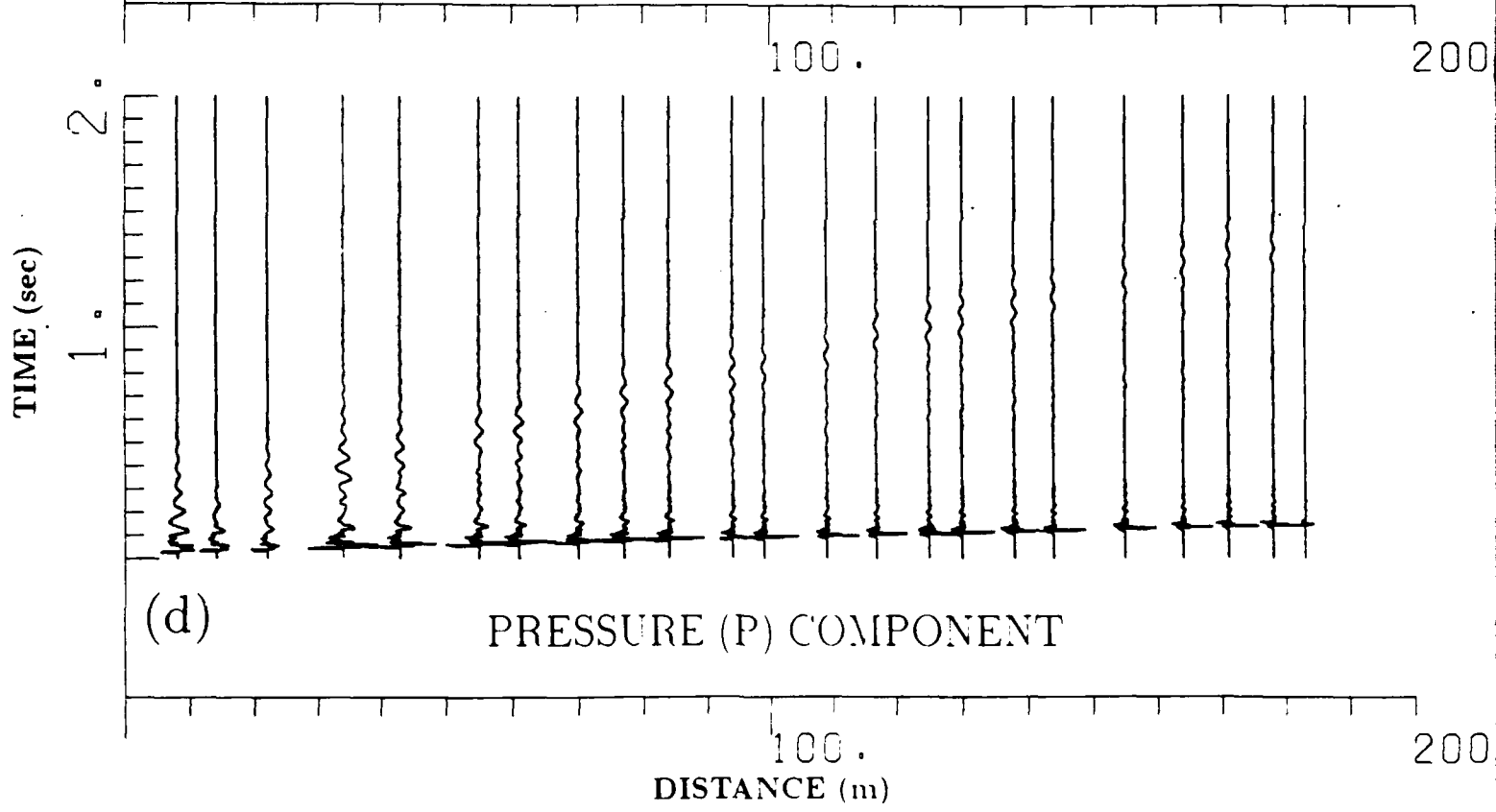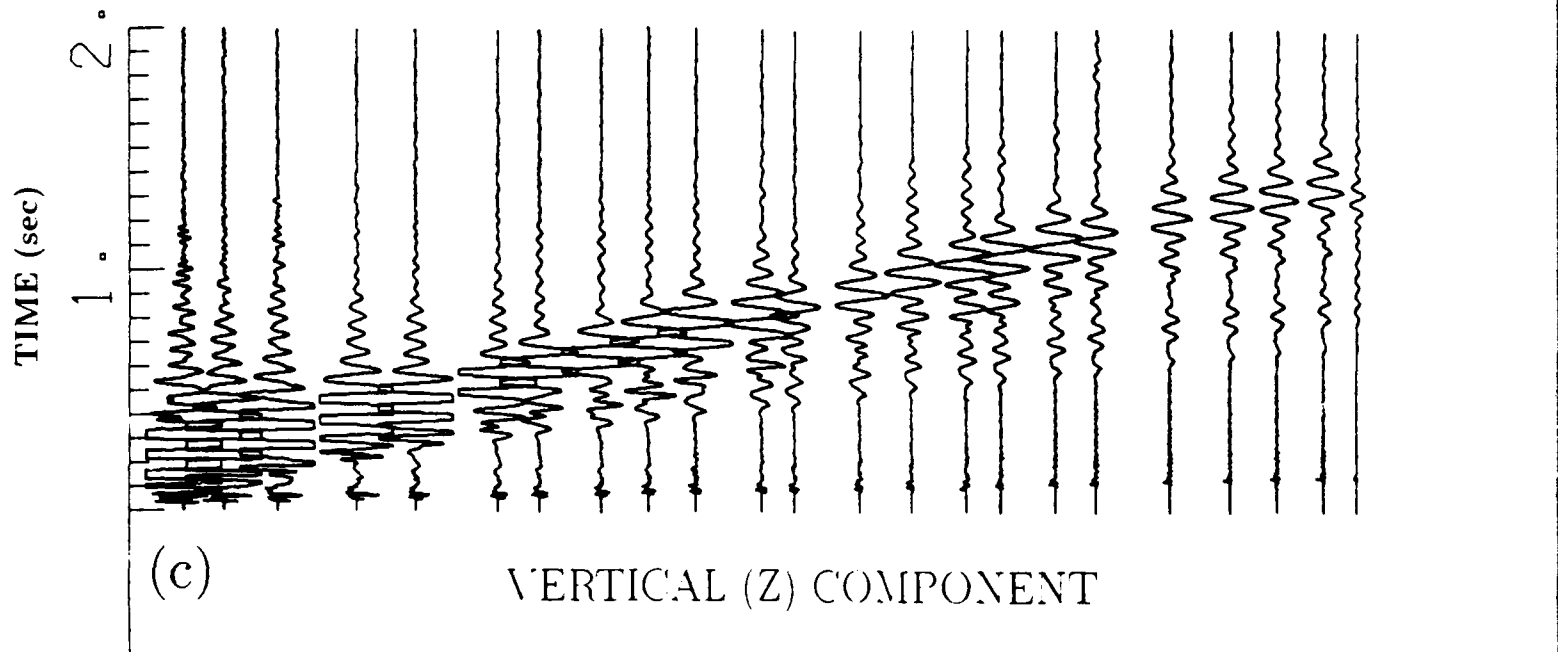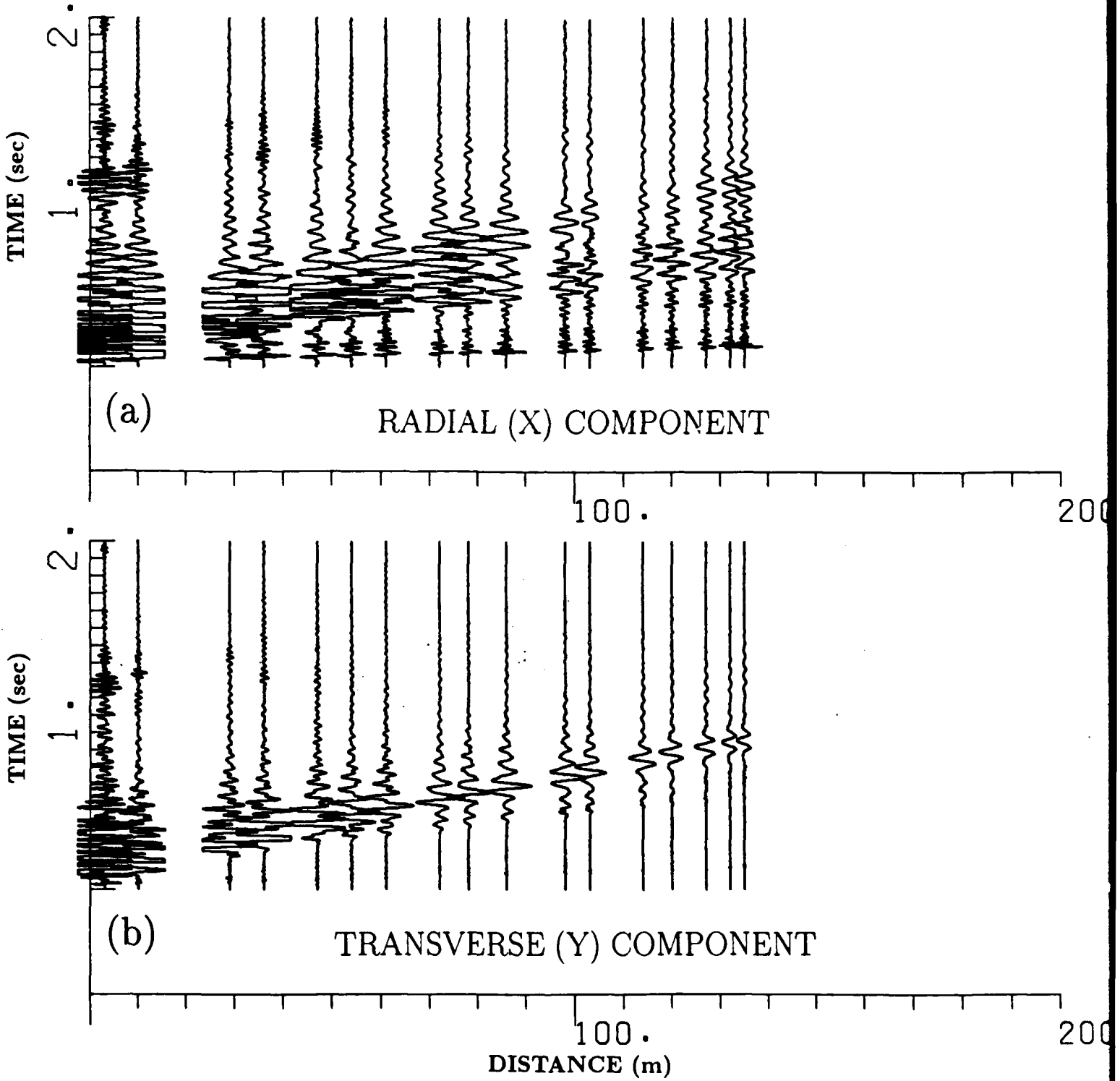
UNFILTERED DATA

Figure 5: Record sections from the short profile. Northwest end of profile is plotted on the right; southeast end is to the left. Compare to Figure 4.

UNFILTERED DATA

(c) VERTICAL (Z) COMPONENT

(d) PRESSURE (P) COMPONENT

DISTANCE (m)
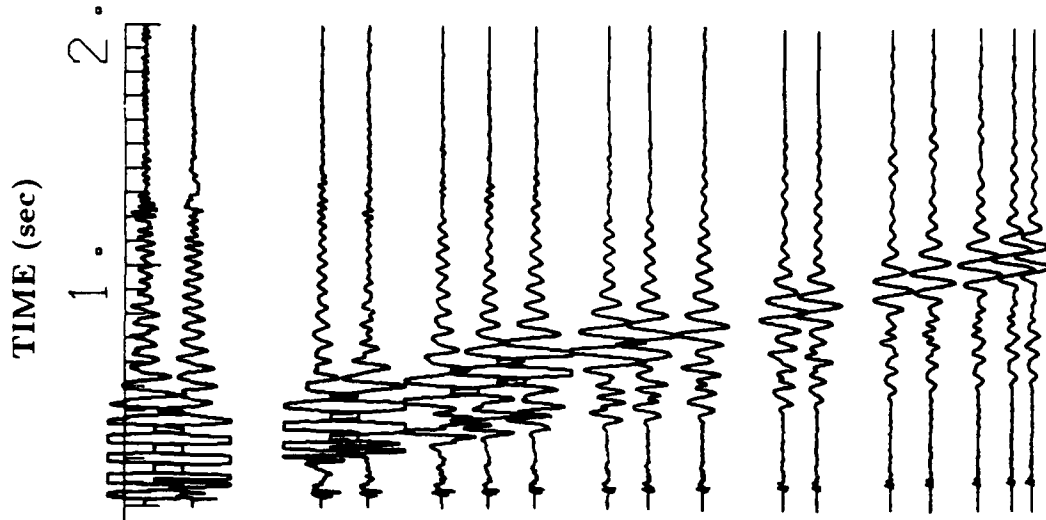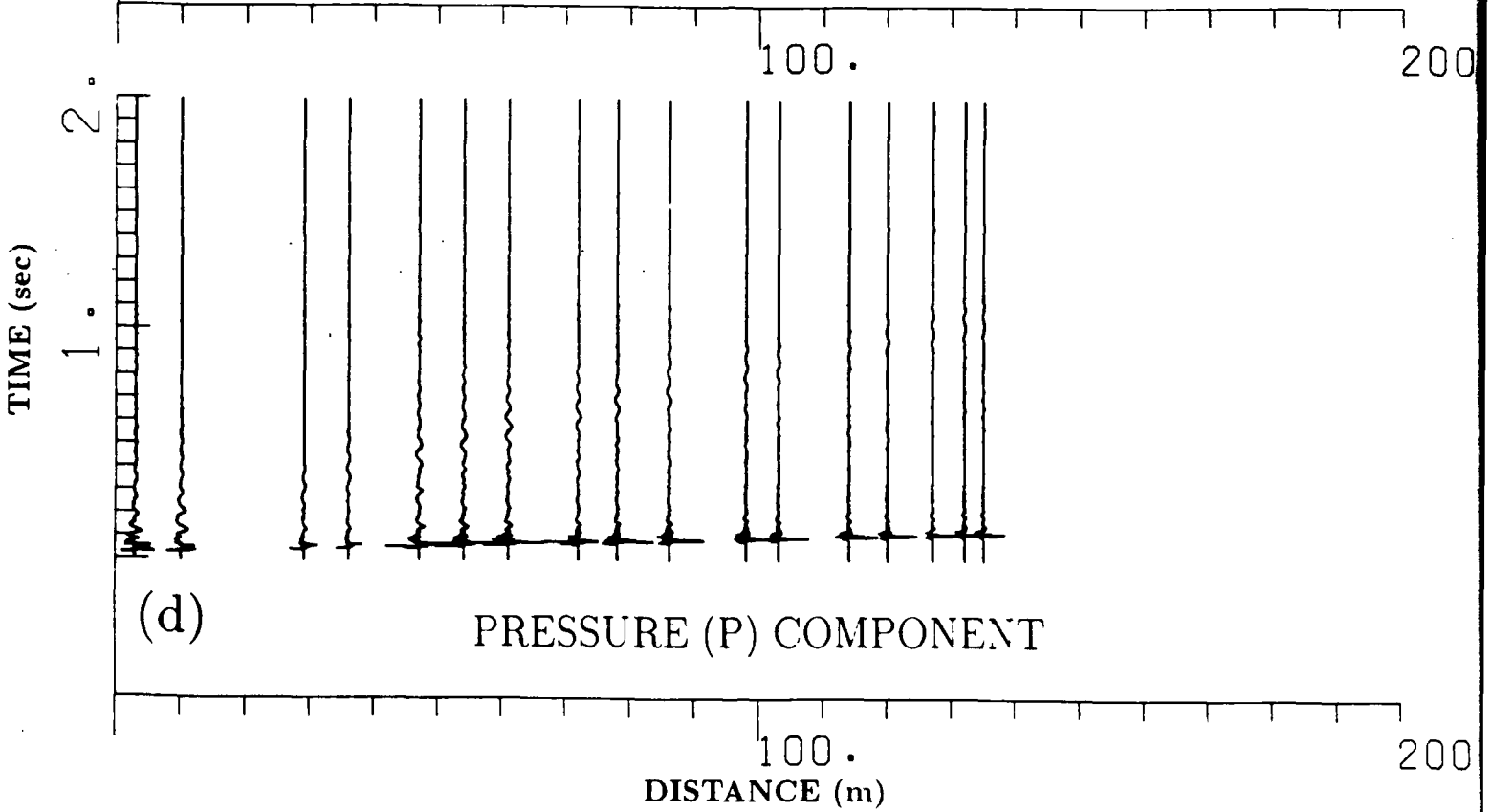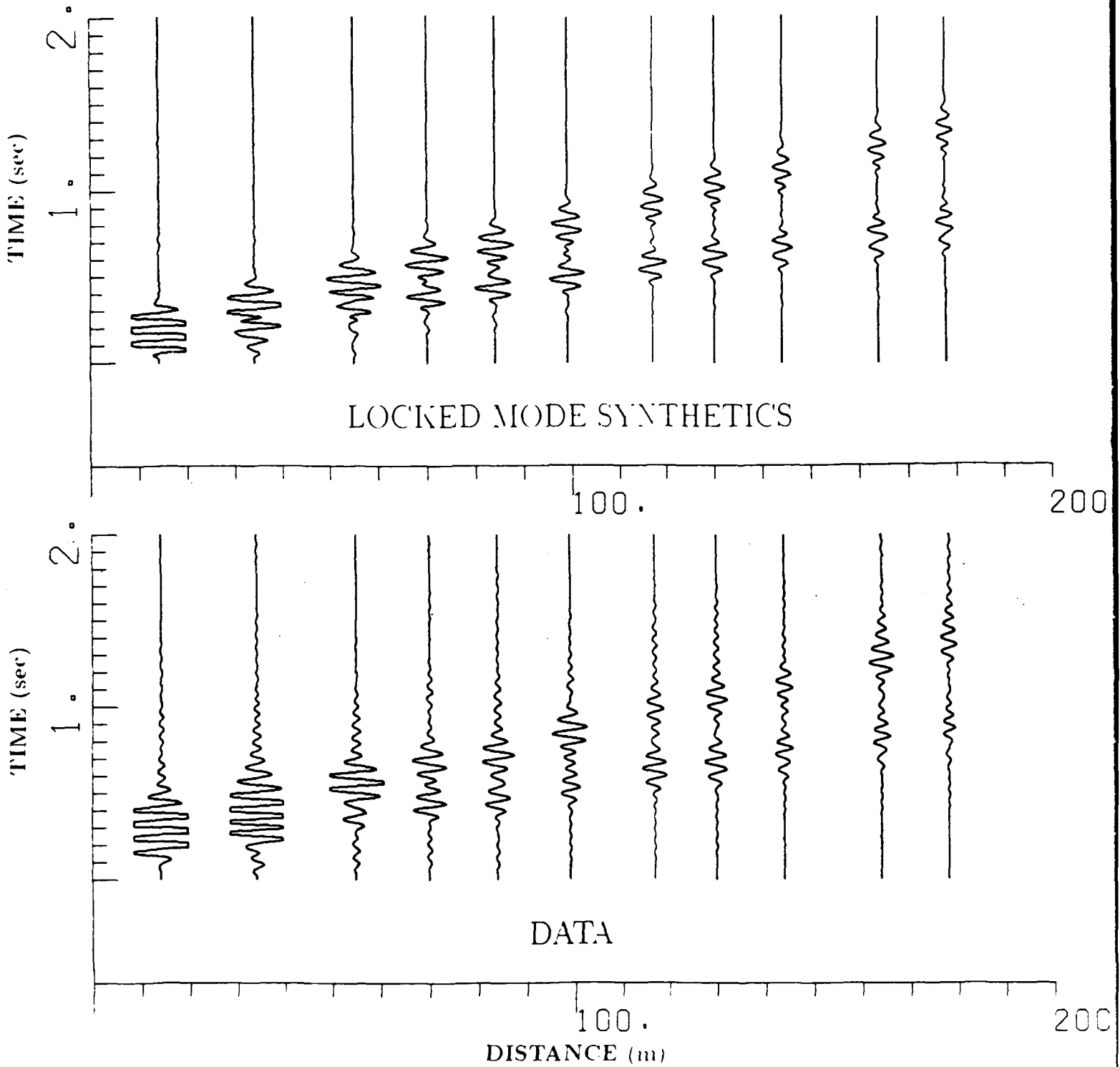
Figure 6: Record sections and "locked mode" synthetic seismograms for horizontal and vertical components of motion for long profile near AMCOR 601i site (Sutton *et al.* 1987). Bandpass filter is from 2–15 Hz. Two different isotropic models were used for X-Z, Y components. (a) Data (bottom) and RAI synthetic seismograms (top) for radial (X) component. (b) Data and RAI synthetic seismograms for transverse (Y) component. (c) Data and RAI synthetic seismograms for vertical (Z) component.

(b) TRANSVERSE (Y) COMPONENT

LOCKED MODE SYNTHETICS

DATA

DISTANCE (m)

(c) VERTICAL (Z) COMPONENT

LOCKED MODE SYNTHETICS

DATA

DISTANCE (m)
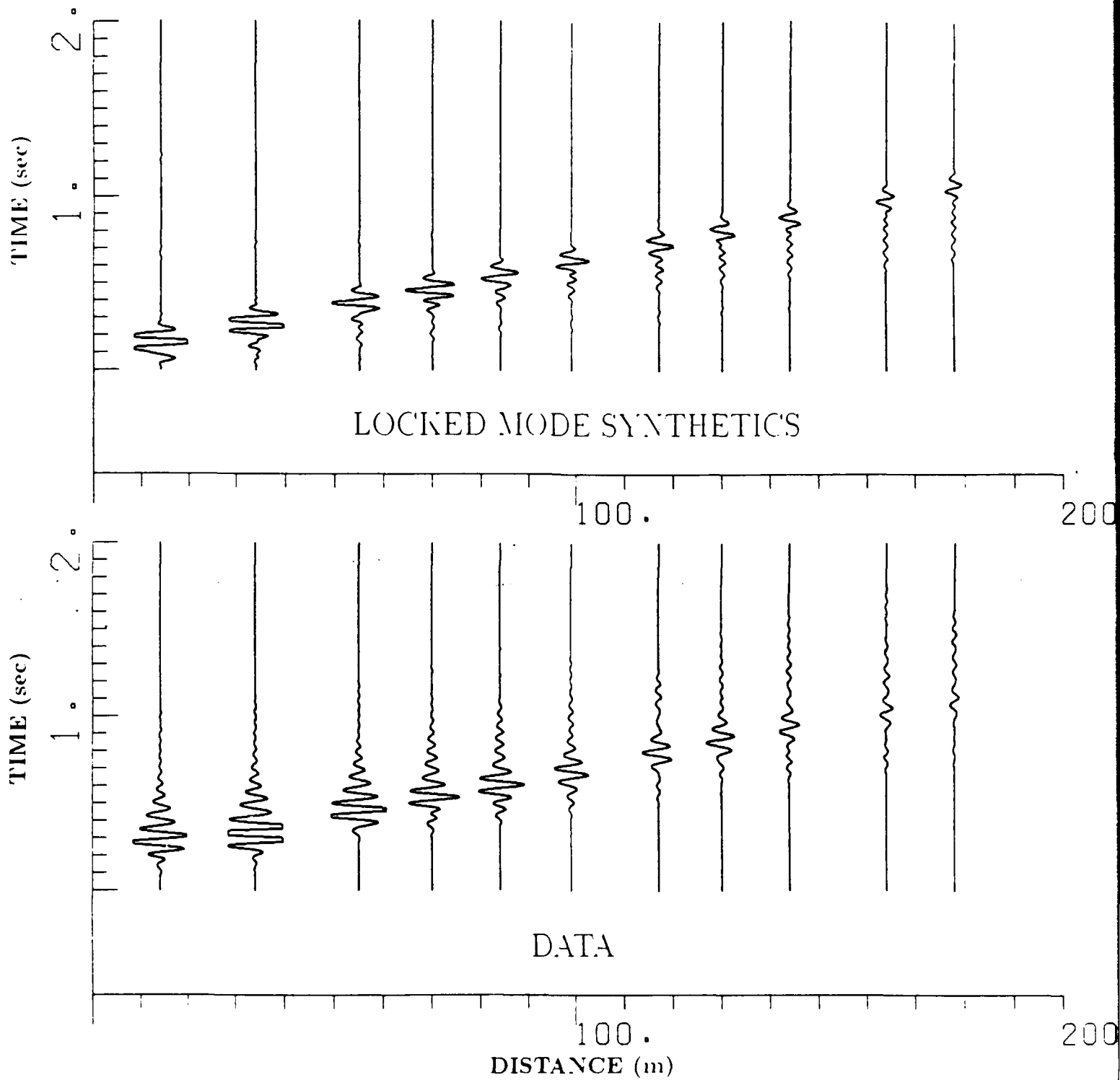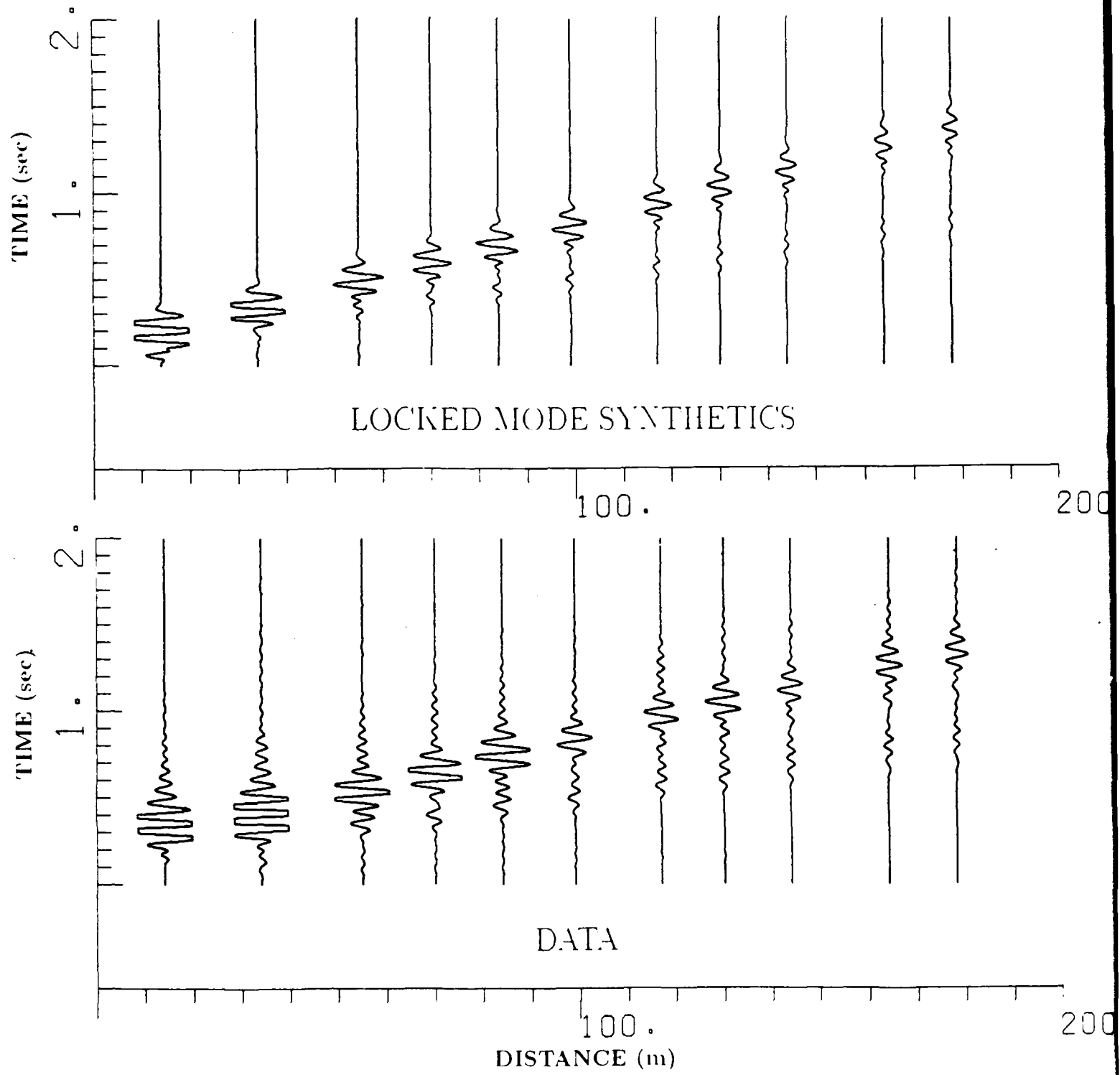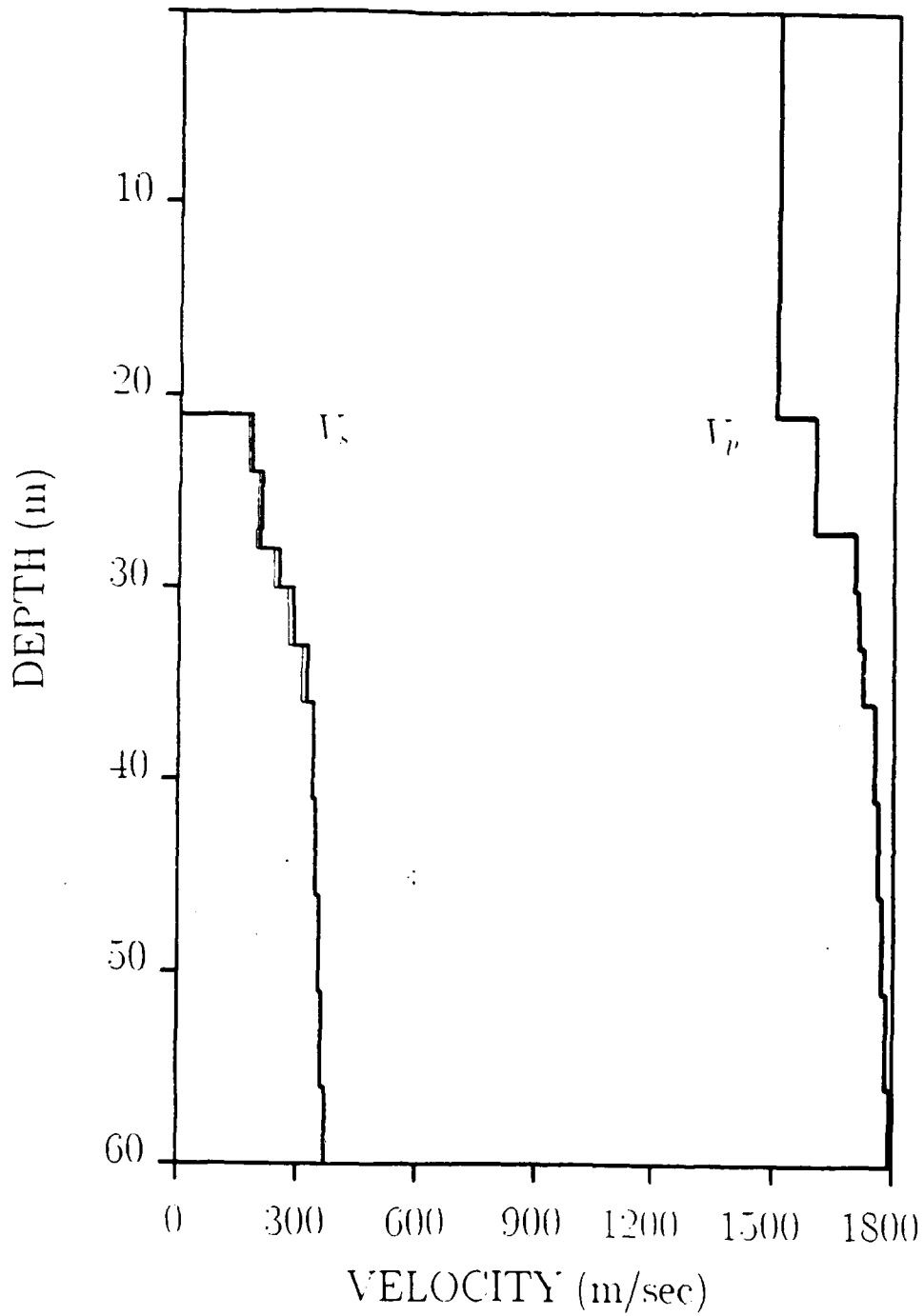
Figure 7: Isotropic velocity models for 1986 RAI/WHOI long profile data, near AMCOR 6011 site. Thin line indicates the RAI model for the X and Z components; bold line shows the RAI model for the Y component. Both models have 21 m of water above the source and receivers. $Q_p \approx \infty$ and $Q_s = 20$ for both models.

(a) 8 m
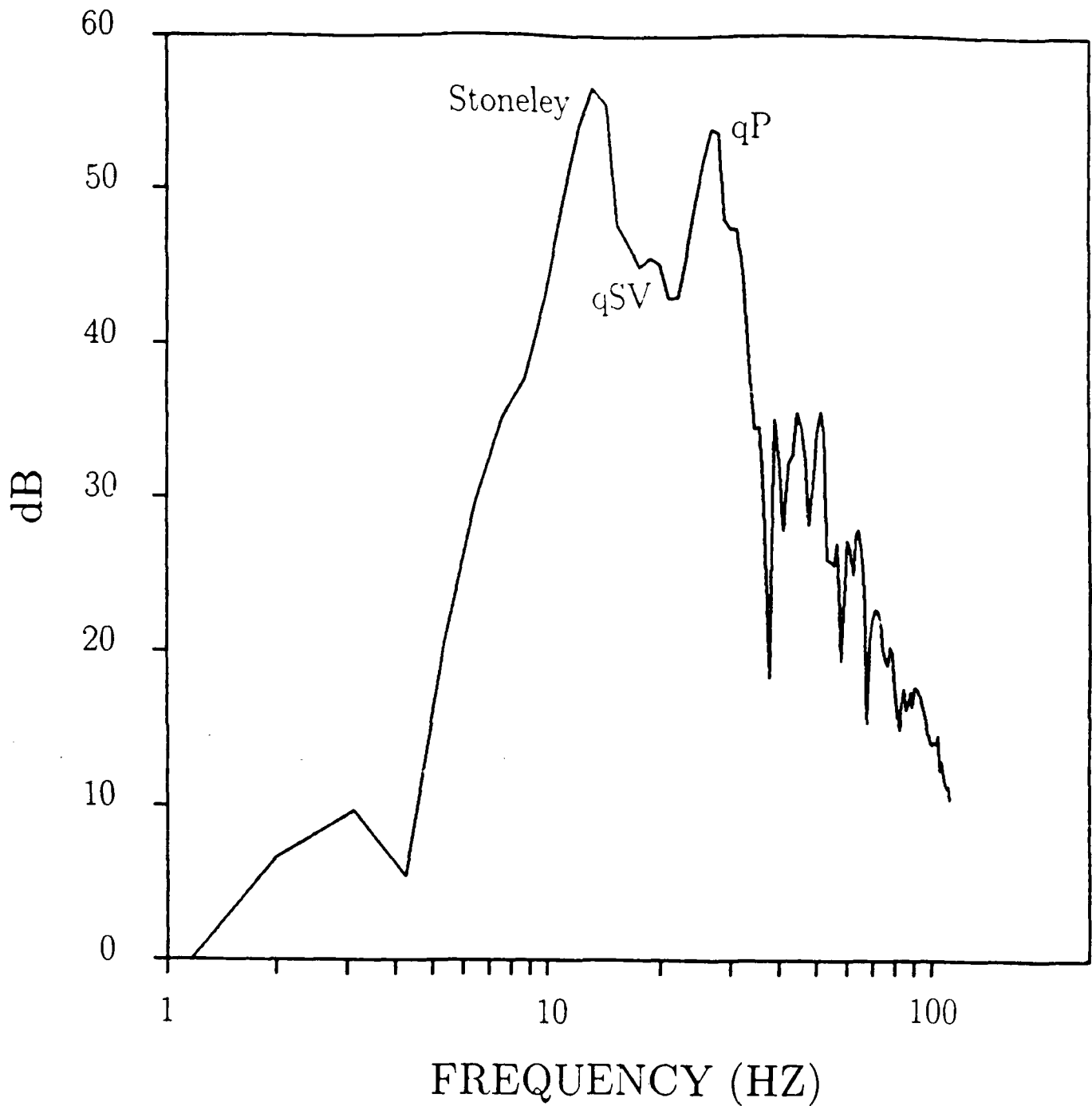
Figure 8: Amplitude vs. frequency, unfiltered vertical component data from the long profile. Amplitudes are in dB, frequencies in Hz. A factor of two change in amplitude corresponds to a 6 dB change. Spectra differ for different ranges, depending on the relative amplitudes of qP, qSV, and Stoneley waves, since the waves have different frequencies. These plots give typical spectra, which were used to determine how to filter the synthetic seismograms. (a) 8 m range. (b) 34 m range. (c) 109 m range.

(b) 34 m
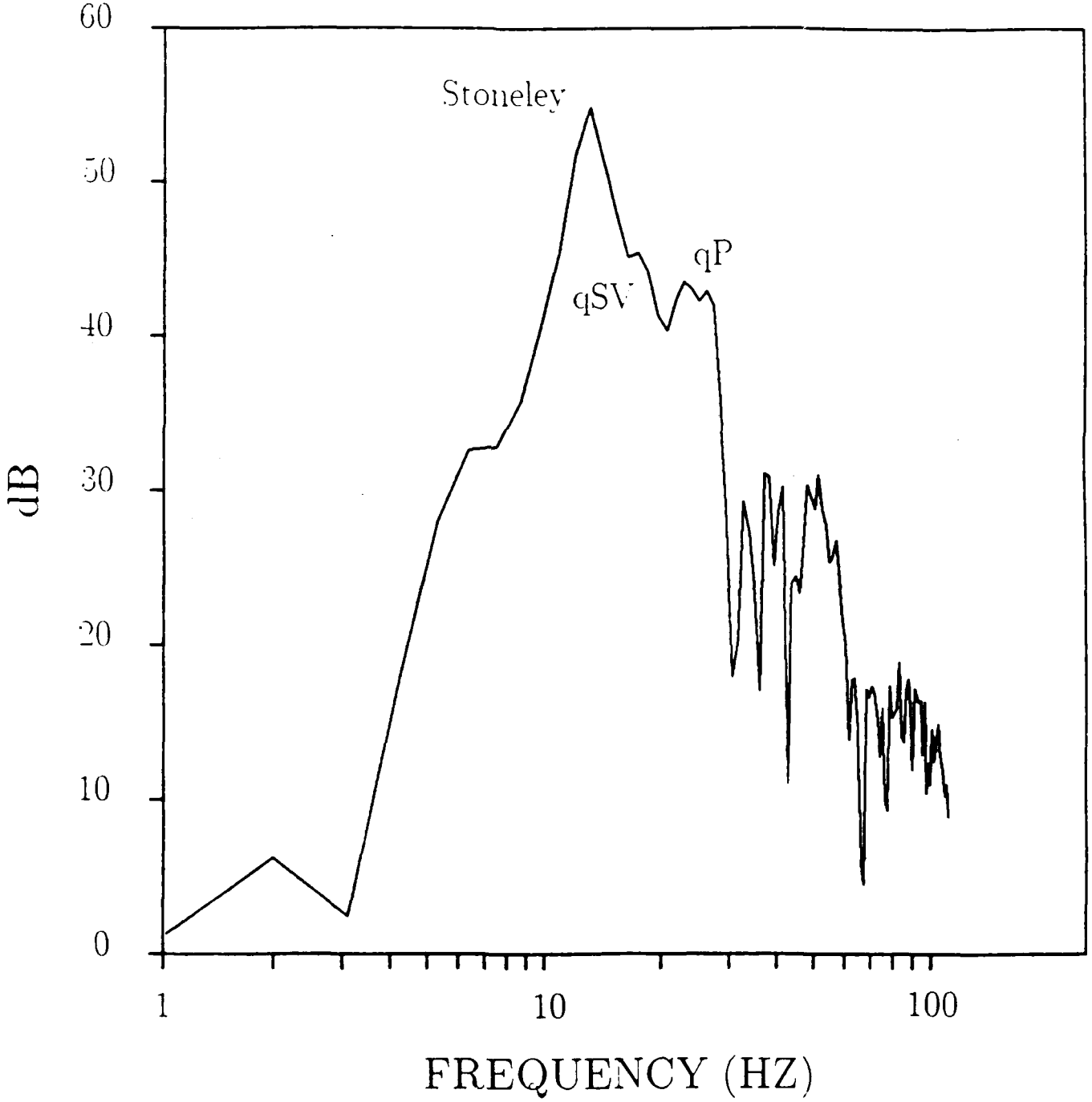
(c) 109 m
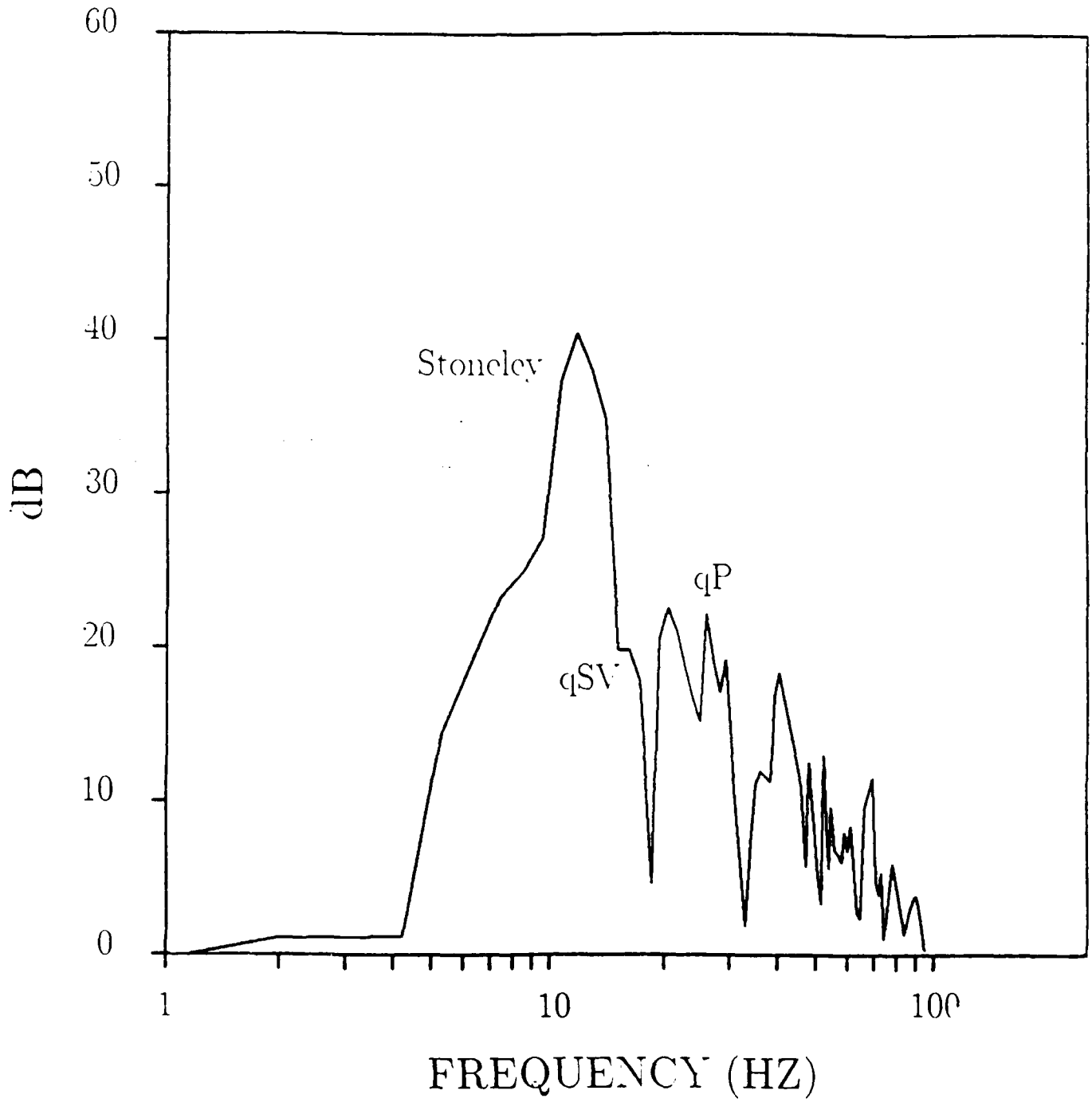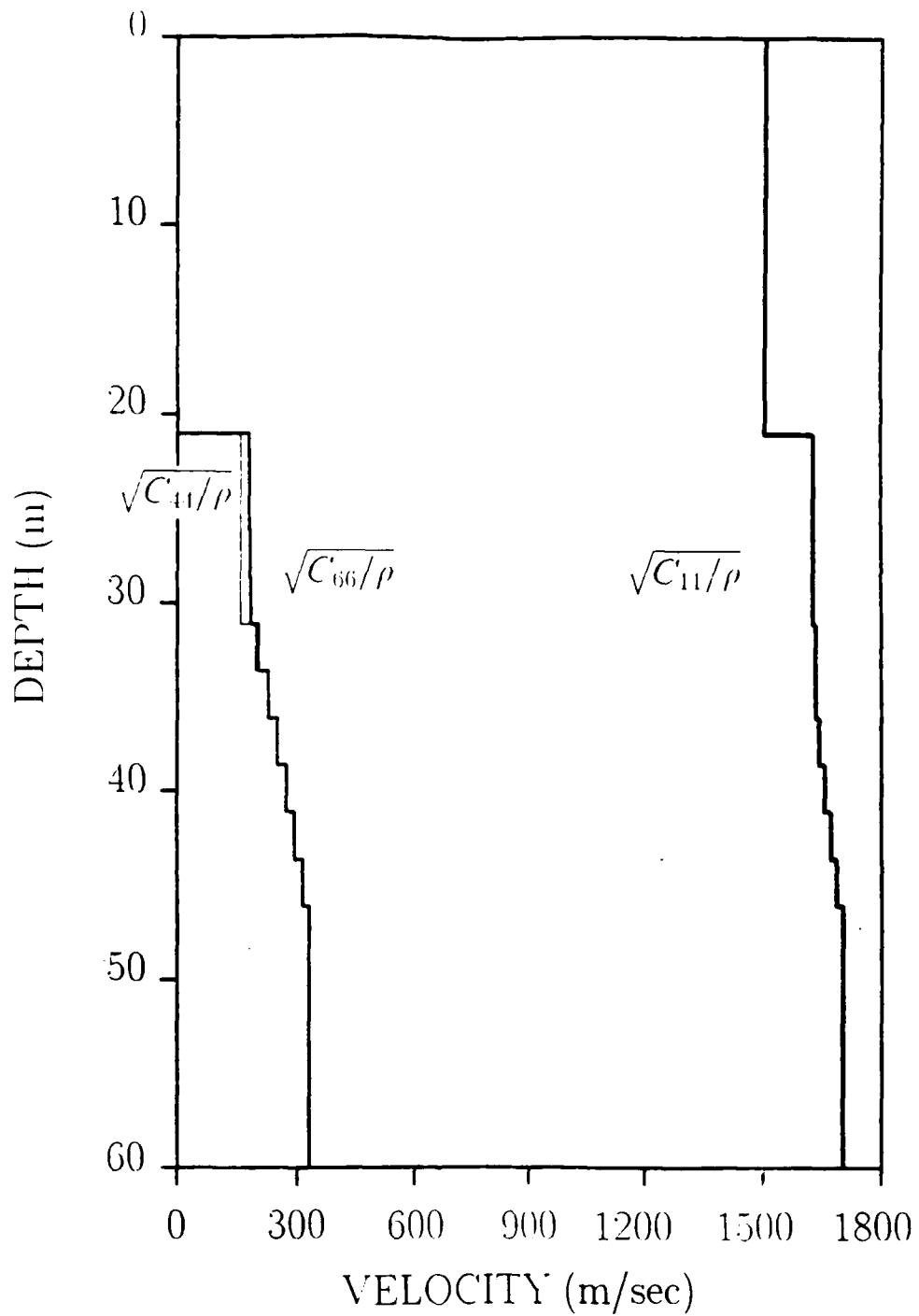
Figure 9: Velocity vs. depth in Table 1 model. for waves travelling parallel to horizontal plane of TI symmetry. Thin line indicates velocity for horizontally-travelling qSV. Bold lines indicate horizontal P-wave velocity and horizontal SH-wave velocity. Complete model for long profile is given in Table 1.
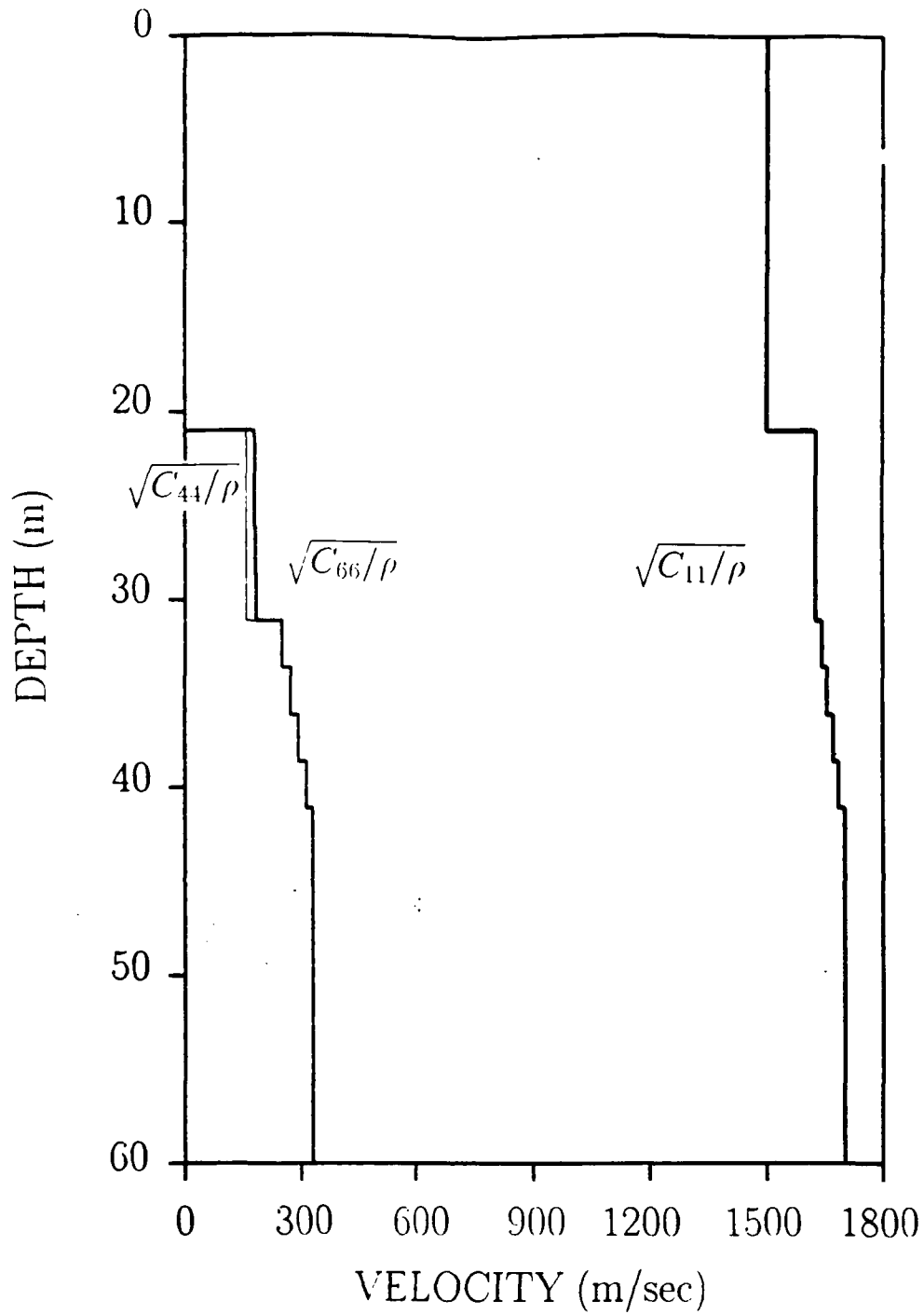
Figure 10: Velocity vs. depth in Table 2 model, for waves travelling parallel to horizontal plane of TI symmetry. Thin line indicates velocity for horizontally-travelling qSV. Bold lines indicate horizontal P-wave velocity and horizontal SH-wave velocity. Complete model for short profile is given in Table 2.

(a) RADIAL (X) COMPONENT

ANISOTROPIC REFLECTIVITY SYNTHETICS

DATA

DISTANCE (m)
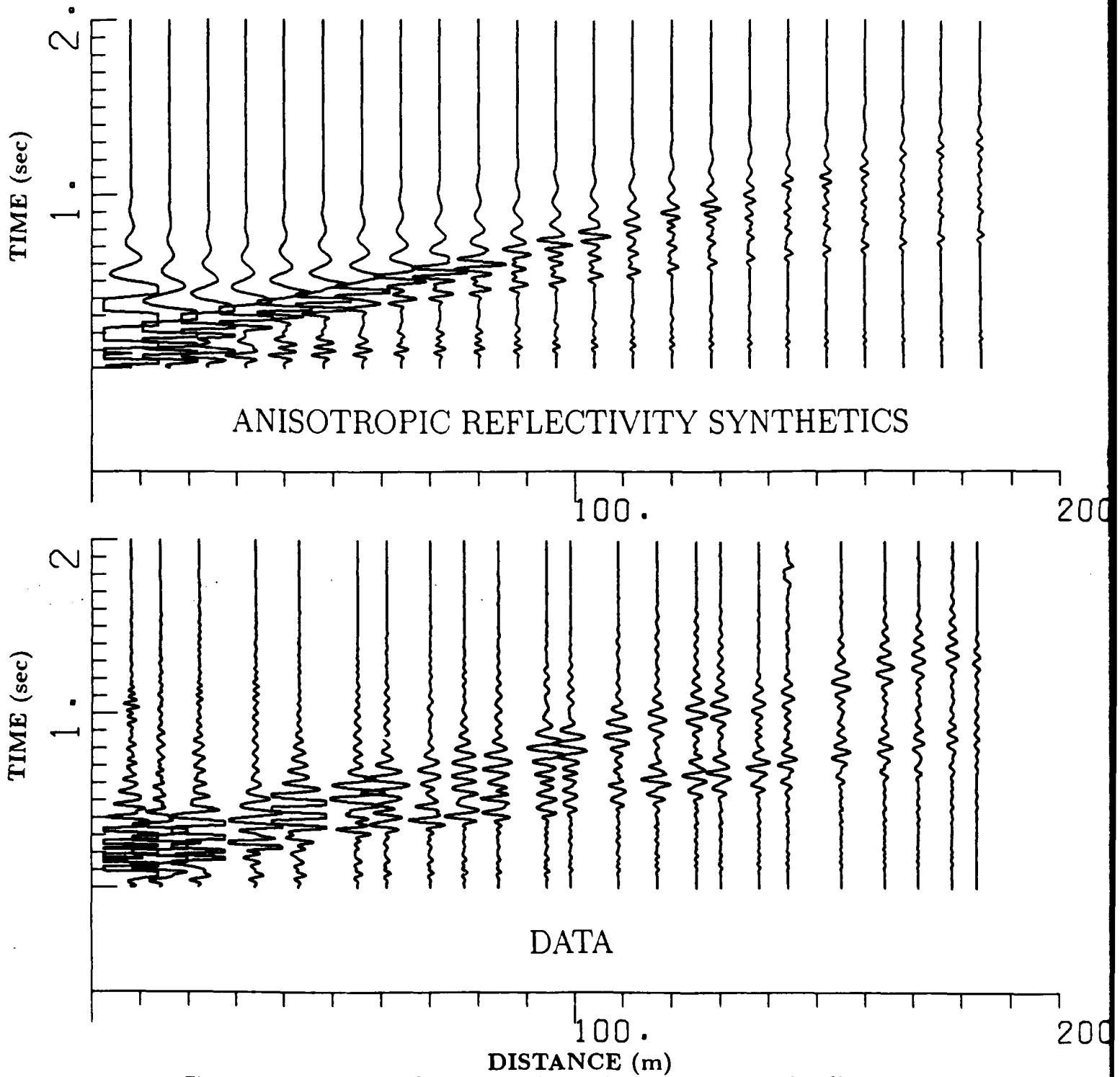
Figure 11: Anisotropic reflectivity synthetic seismograms compared to filtered data for long profile. Data and synthetics were filtered using a 4–25 Hz bandpass filter. Unreduced times in seconds, ranges in meters. (a) Synthetics (top) and data (bottom) for X component. (b) Y component. (c) Z component.

(b) TRANSVERSE (Y) COMPONENT

ANISOTROPIC REFLECTIVITY SYNTHETICS

DATA

DISTANCE (m)

(c) VERTICAL (Z) COMPONENT

ANISOTROPIC REFLECTIVITY SYNTHETICS

100.   200

DATA

100.   200

DISTANCE (m)

(a) RADIAL (X) COMPONENT

ANISOTROPIC REFLECTIVITY SYNTHETICS

DATA

DISTANCE (m)
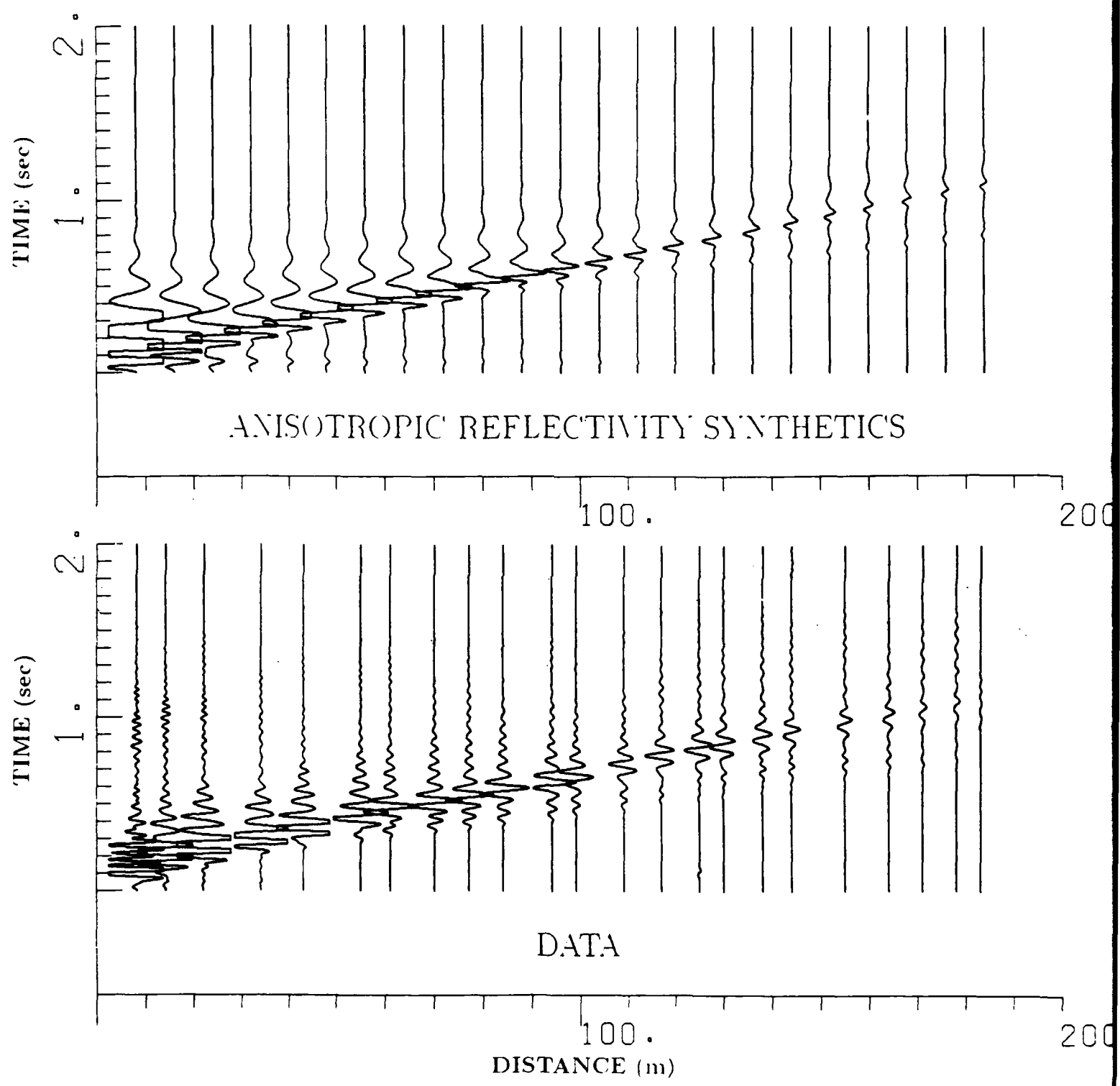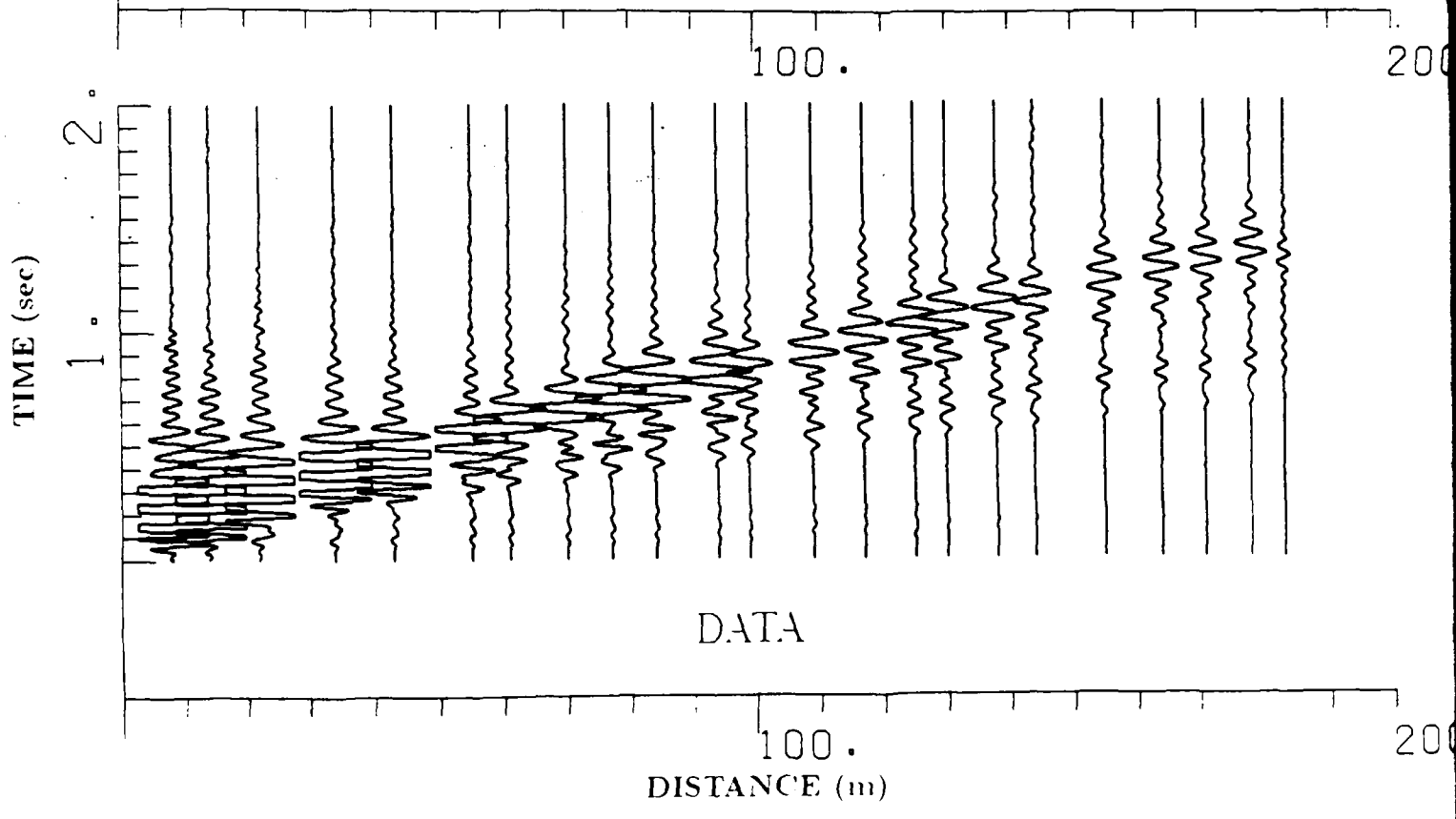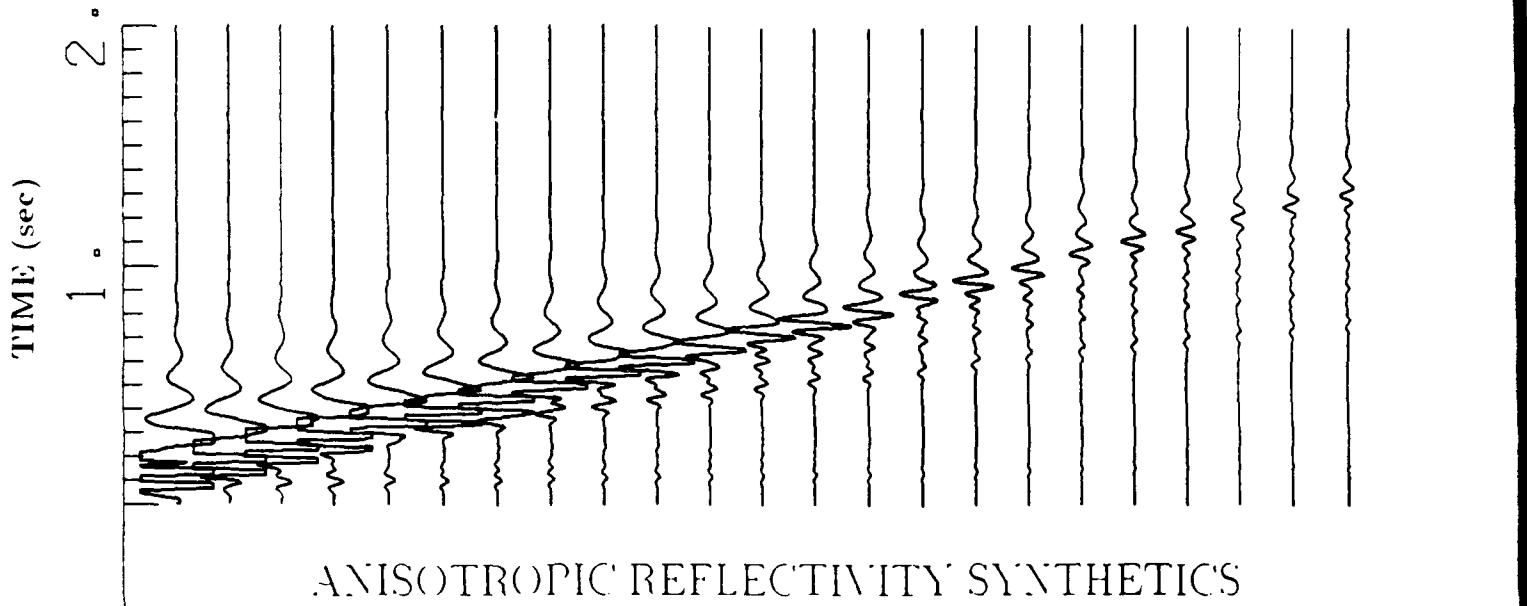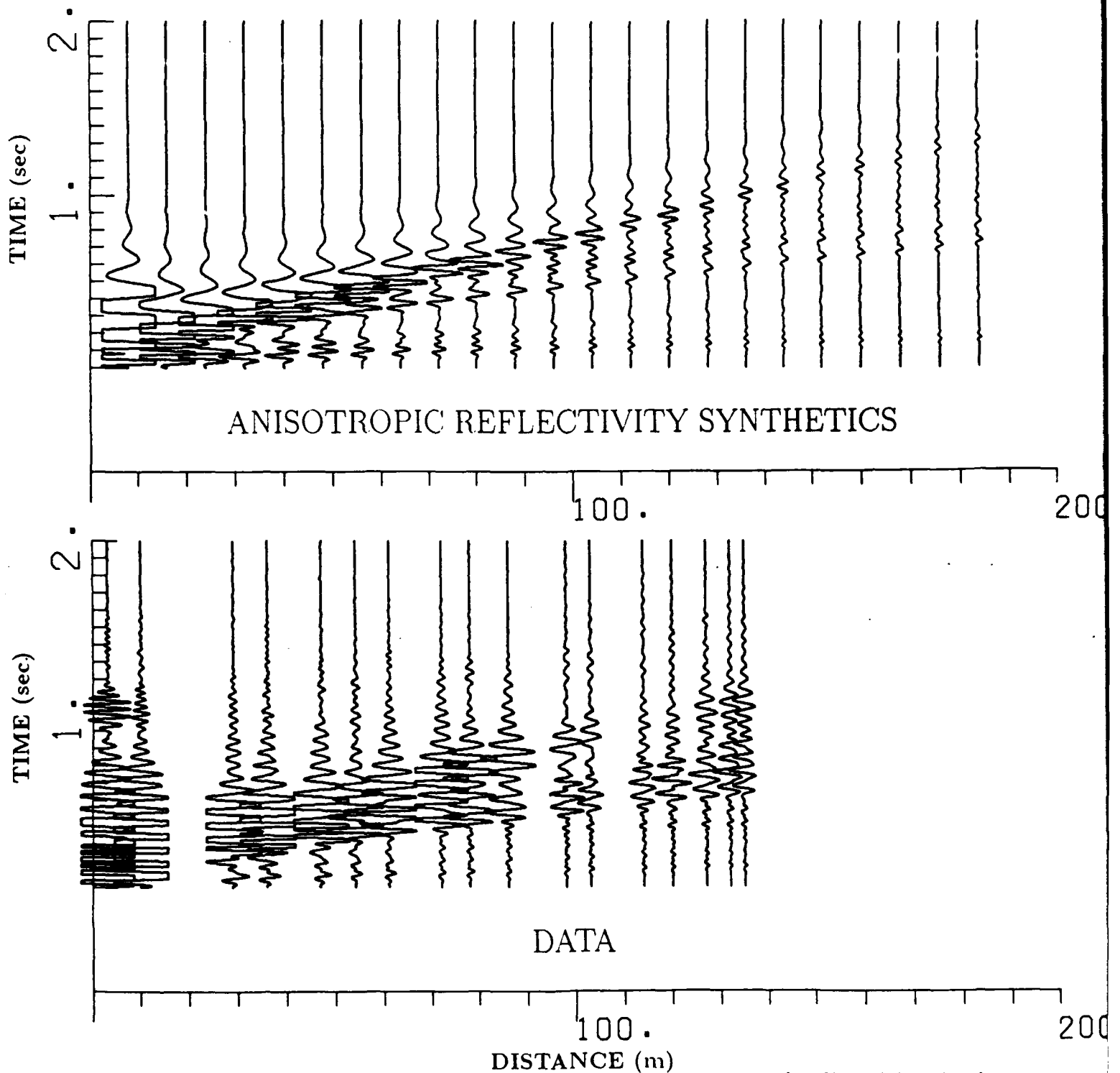
Figure 12: Anisotropic reflectivity synthetic seismograms compared to filtered data for short profile. Data and synthetics were filtered using a 4–25 Hz bandpass filter. Unreduced times in seconds, ranges in meters. (a) Synthetics (top) and data (bottom) for X component. (b) Y component. (c) Z component.

(b) TRANSVERSE (Y) COMPONENT

ANISOTROPIC REFLECTIVITY SYNTHETICS

DATA

DISTANCE (m)

(c) VERTICAL (Z) COMPONENT

ANISOTROPIC REFLECTIVITY SYNTHETICS

DATA

DISTANCE (m)

PHASE SLOWNESS
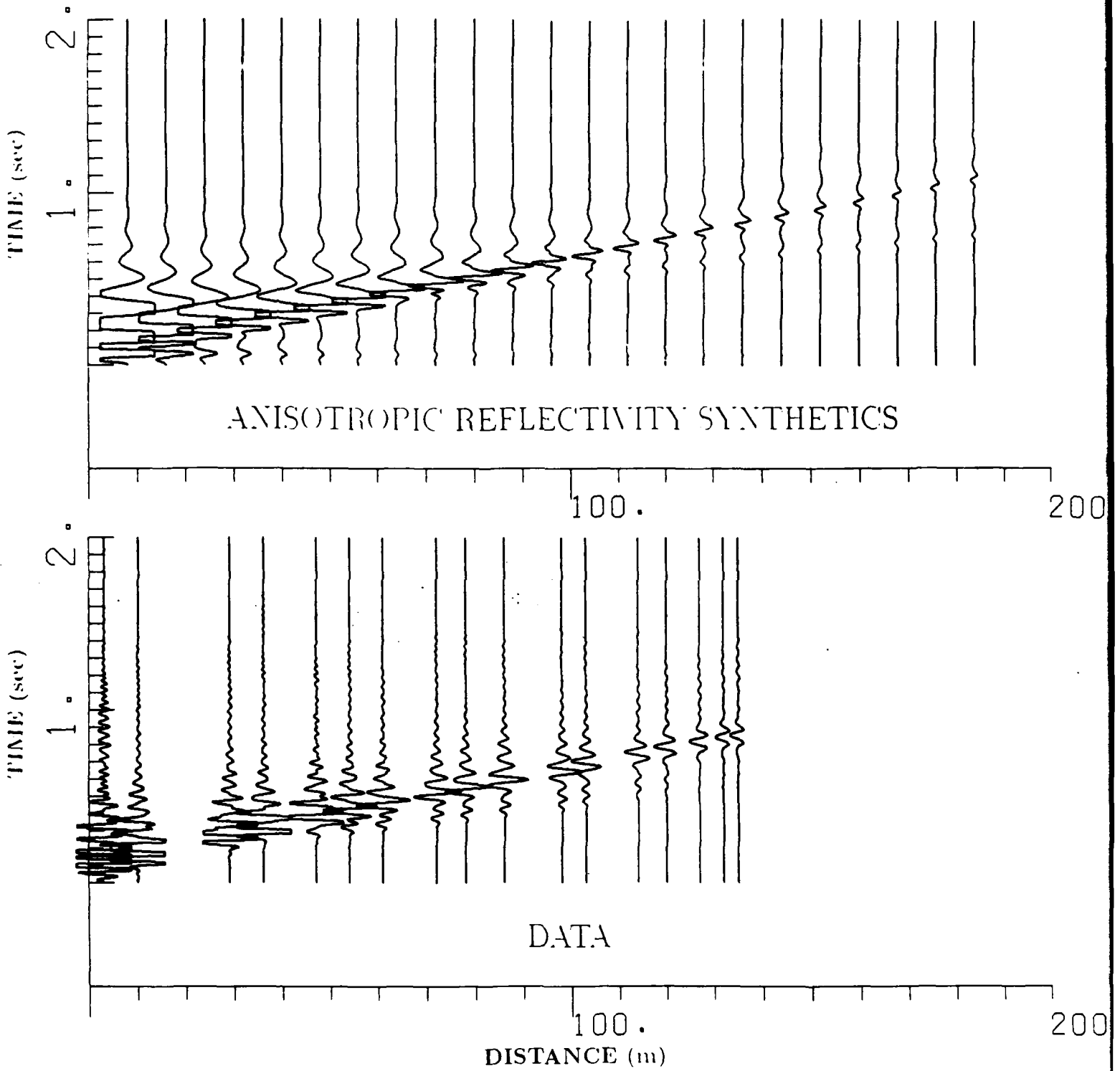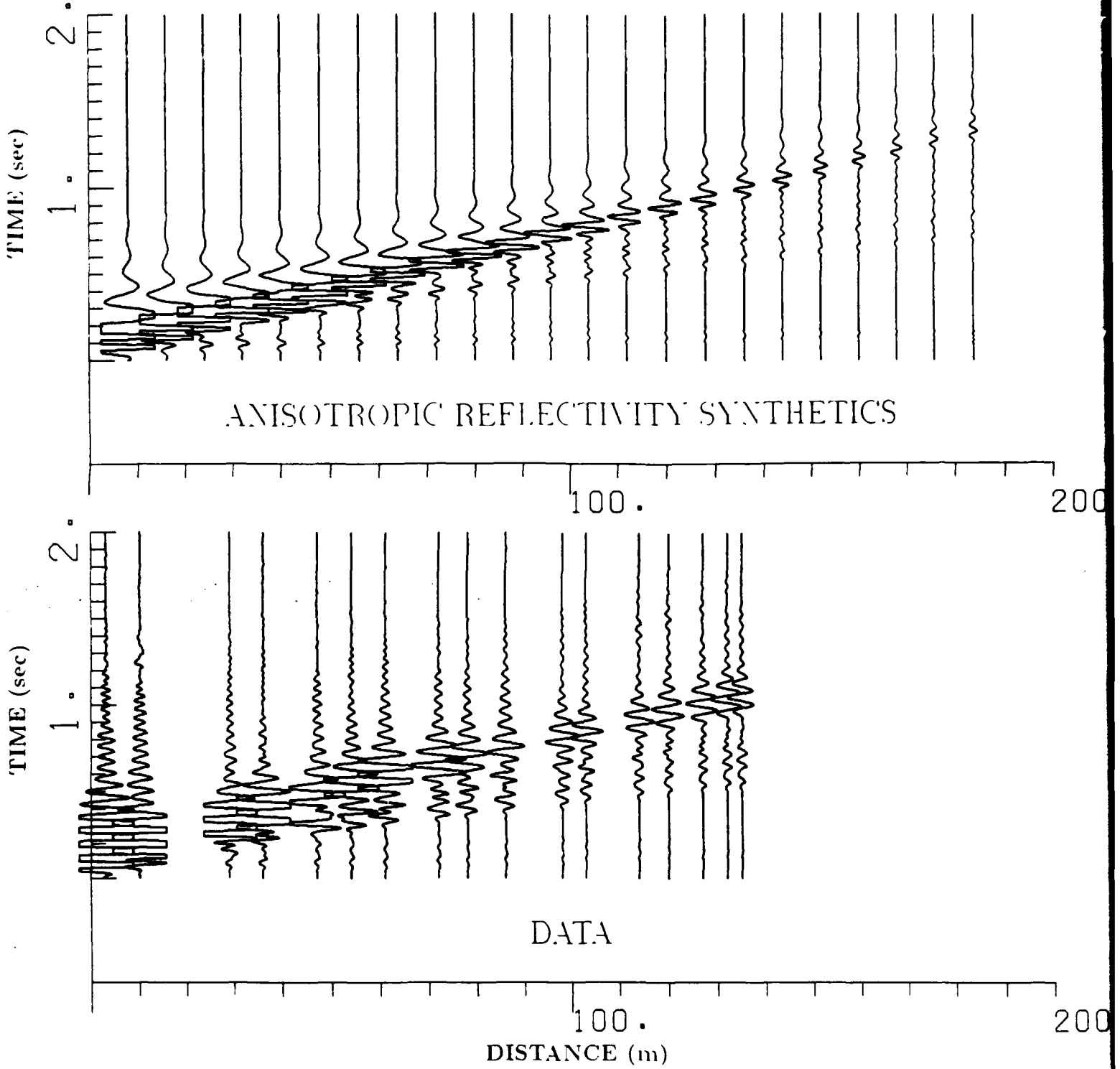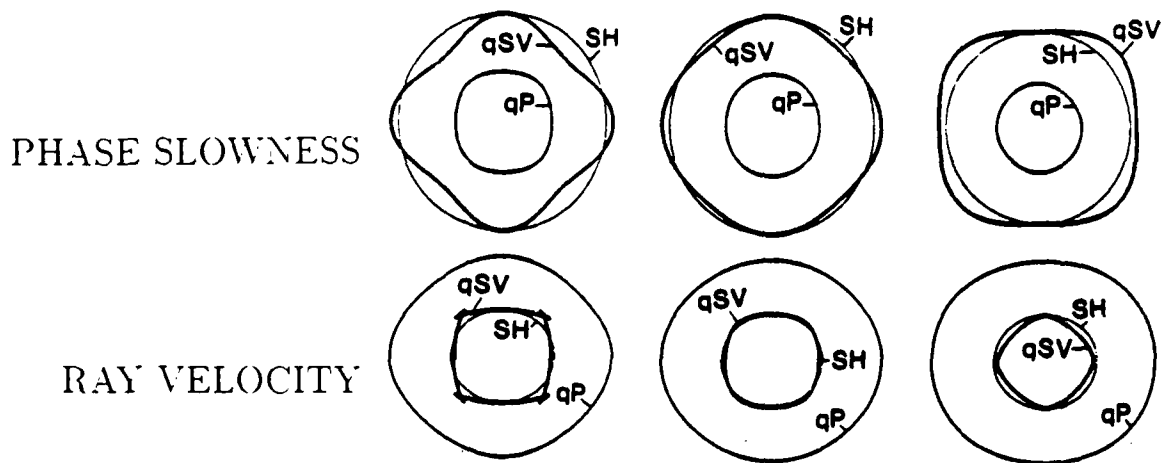
RAY VELOCITY

Figure 13: Effect of C_{13} on wavefront shapes. Cross sections of slowness and velocity surfaces, through $Y = 0$ plane. Since velocity is proportional to distance a wave travels in unit time, velocity surfaces show wavefront shapes. Slowness curves (top) and velocity curves (below) change as the value of C_{13} is raised. Curves on left have lowest value of C_{13}. Values of the other four elastic stiffnesses were held constant. (Adapted from Miller 1987).
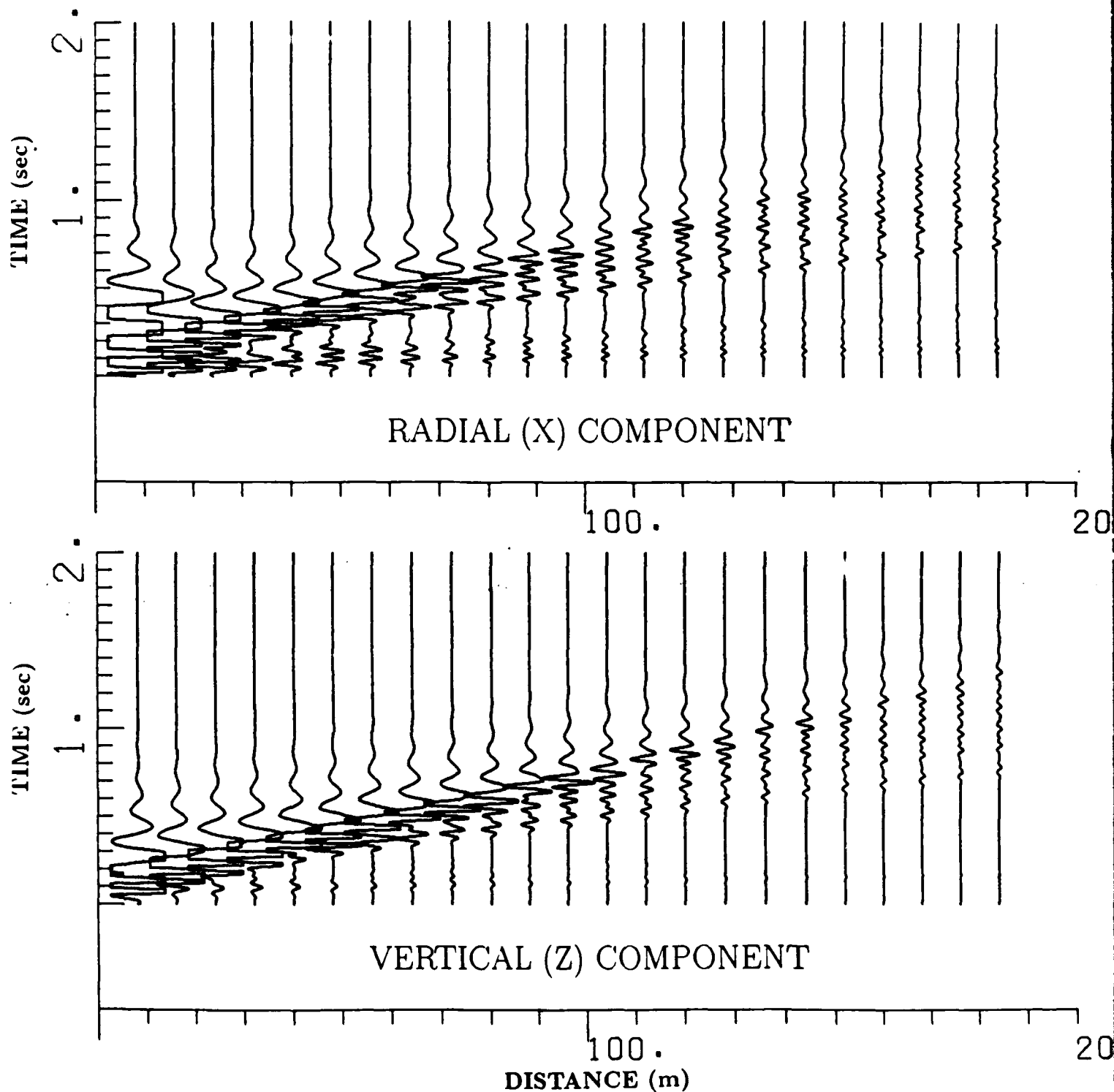
Figure 14: Effect of C_{13} on synthetic seismograms. Values of C_{13} from Table 1 for the long profile were perturbed by 0.06 GPa, in the top 10 m of the sediments. Then new synthetic seismograms were computed. Compare to Figure 11, X and Z components.
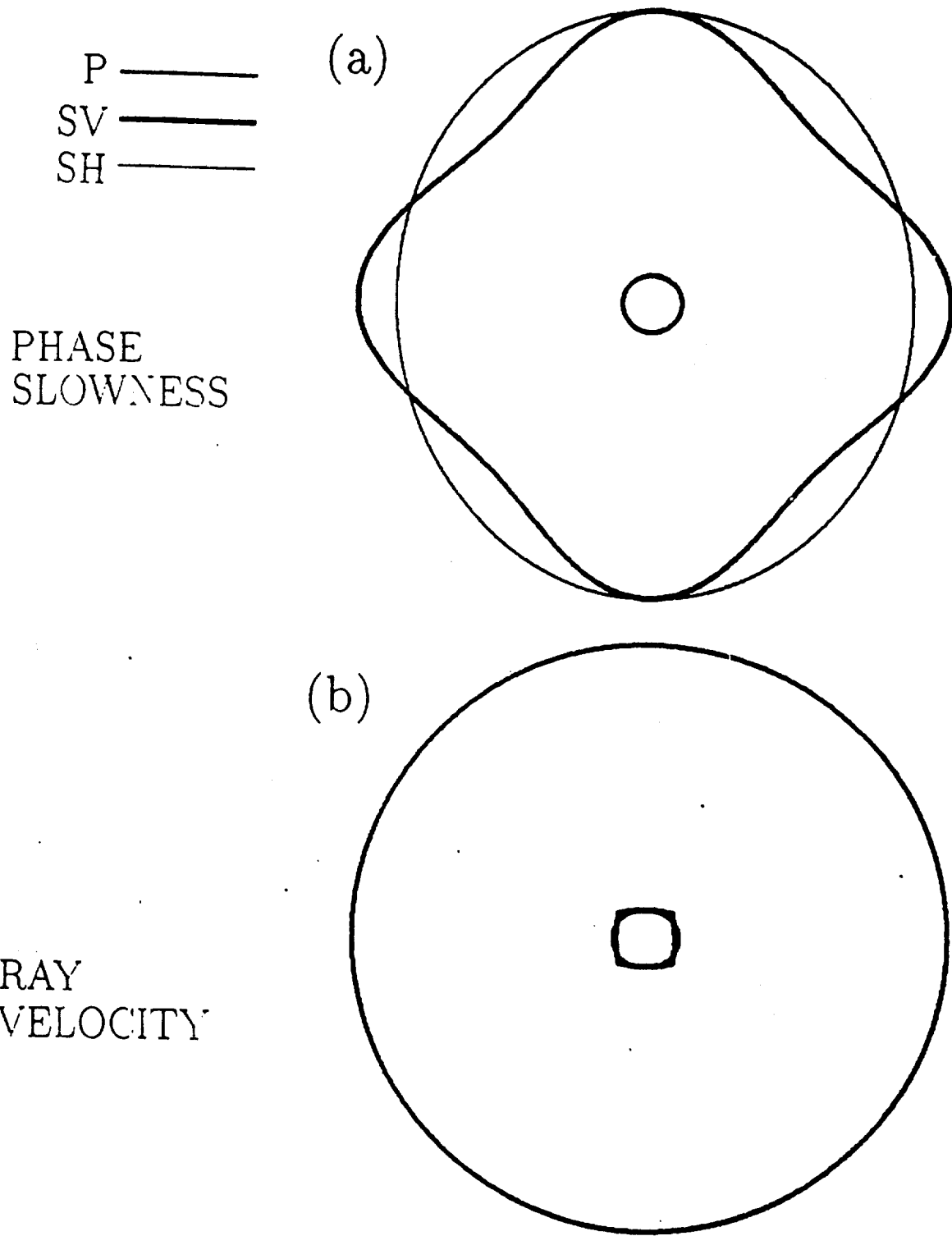
Figure 15: Cross sections of slowness and velocity surfaces, through $Y = 0$ plane. (a) Slowness surface, average for top 10 m of sediments for model in Table 1. (b) Velocity surface, average for top 10 m of sediments.